Petroleum Science 23 (2026) 7355–7373

Contents lists available at ScienceDirect

Petroleum Science

journal homepage: www.keaipublishing.com/en/journals/petroleum-science

Original paper

Numerical simulation of fracture height growth in deep shale reservoirs based on CDEM-THM

Hai-Yang Wang [a,b], Ming Chen [a,b,*], Tian-Kui Guo [a,b], Yi Zhang [c,**], Ji-Wei Wang [d], Xin-Min Ge [e], Bo Chen [f], Feng-Shou Zhang [g]

[a] School of Petroleum Engineering, China University of Petroleum (East China), Qingdao, 266580, Shandong, China
[b] National Key Laboratory of Deep Oil and Gas, China University of Petroleum (East China), Qingdao, 266580, Shandong, China
[c] State Key Laboratory of Deep Earth and Mineral Exploration, Chinese Academy of Geological Sciences, Beijing, 100037, China
[d] School of Safety Engineering, China University of Mining and Technology, Xuzhou, 221116, Jiangsu, China
[e] School of Geosciences, China University of Petroleum (East China), Qingdao, 266580, Shandong, China
[f] PetroChina Changqing Oilfield Company, Xi'an, 710018, Shaanxi, China
[g] College of Civil Engineering, Tongji University, Shanghai, 200092, China

ARTICLE INFO

Article history:
Received 1 February 2026
Received in revised form
26 April 2026
Accepted 18 June 2026
Available online 24 June 2026

Edited by Meng-Jiao Zhou

Keywords:
Thermo-hydro-mechanical coupling
Bedding plane
Fracture propagation
Continuum-discontinuum element method
Thermal stress

ABSTRACT

The influence of thermal stress during hydraulic fracturing in deep shale reservoirs cannot be neglected, and the mechanism of fracture height propagation under the combined effects of thermal stress and bedding planes remains unclear. The continuous-discontinuous element method was used to develop a three-dimensional thermo-hydro-mechanical coupled hydraulic fracturing model (CDEM-THM) to investigate the fracture height growth mechanisms and hydraulic fracture-bedding plane interaction behaviors under the combined effects of thermal stress, vertical stress difference, and bedding plane cohesion. The results show that thermal stress significantly alters the original in-situ stress field and serves as a key factor controlling fracture height growth and the interaction mode between hydraulic fractures and bedding planes. By acting as tensile stress, thermal stress reduces the three in-situ principal stresses and lowers the fracturing pressure, resulting in increased fracture width, reduced fracture height and length, and the generation of secondary fractures. Thermal stress reduces the normal stress above bedding planes, thereby lowering the activation difficulty and enabling hydraulic fractures to activate parts of the bedding planes while crossing them. When the vertical stress difference is small, the promoting effect of thermal stress on the fracture's ability to cross bedding planes becomes more pronounced, causing the interaction mode to evolve from propagation along bedding planes to partial activation and crossing. In reservoirs with high temperatures and thermal expansion coefficients, the generated high thermal stress plays a positive role in the vertical extension of fracture and the formation of complex fracture networks. A larger vertical stress difference or bedding plane cohesion weakens the promoting effect of thermal stress on bedding plane activation. The findings of this study provide a theoretical basis for forecasting fracture propagation morphology in field operations targeting deep shale reservoirs.

© 2026 The Authors. Publishing services by Elsevier B.V. on behalf of KeAi Communications Co. Ltd. This is an open access article under the CC BY license (http://creativecommons.org/licenses/by/4.0/).

1. Introduction

The steady reduction in conventional oil and gas availability has shifted increasing attention toward the development of unconventional resources. As a core component of unconventional resources, shale oil and gas hold strategic significance in the ongoing global energy transition (Lei et al., 2021; Wang et al., 2022a; Martyushev et al., 2024). Vertically distributed bedding planes (BPs) are a characteristic feature of shale reservoirs. As weak interfaces within the rock mass, they can significantly control

* Corresponding author.
** Corresponding author.
E-mail addresses: chenmingfrac@163.com (M. Chen), shidazhangyang@163.com (Y. Zhang).

Peer review under the responsibility of China University of Petroleum (Beijing).

https://doi.org/10.1016/j.petsci.2026.06.036
1995-8226/© 2026 The Authors. Publishing services by Elsevier B.V. on behalf of KeAi Communications Co. Ltd. This is an open access article under the CC BY license (http://creativecommons.org/licenses/by/4.0/).

hydraulic fracture (HF) height by influencing fracture behavior—such as crossing, arresting, or offsetting—when the fracture extends to a bedding plane (BP) (Taleghani et al., 2016; Zhang et al., 2021). As extraction technologies for shallow shale gas gradually mature, deeper shale development is emerging as a critical direction for technological breakthroughs (Zou et al., 2021; Nie et al., 2023). With increasing reservoir depth, formation temperature becomes a non-negligible factor in fracture growth (Lin et al., 2024; Zhao et al., 2025). When low-temperature fracturing fluid enters high-temperature formations, thermal stresses are generated, substantially influencing hydraulic fracture expansion and its interaction with bedding planes. Therefore, investigating the mechanism of fracture height growth under the combined effects of thermal stress and bedding planes is of great significance.

The effect of BPs on hydraulic fracture growth in unconventional reservoirs has been a continuous research focus. Qu et al. (2022, 2023) conducted liquid nitrogen fracturing experiments on shale samples containing BPs. The results indicate that the thermal effects generated by the injection of extremely low-temperature liquid nitrogen into the reservoir can lower the breakdown pressure, and can thermally induce pre-existing fractures, BPs, and secondary pores in shale. Xie et al. (2025) conducted high-temperature fracturing experiments on granite and found that a larger temperature difference between the injected fluid and the rock is favorable for the activation of pre-existing fractures under the combined effects of thermal stress and fluid pressure. These studies provide direct experimental evidence for the influence of thermal stress on hydraulic fracture–bedding plane interaction. However, constrained by factors such as small experimental scale and difficulties in quantitative analysis, numerical simulation has become an effective tool for researchers to investigate these issues. Some studies primarily focus on the evolutionary characteristics of BPs, aiming to elucidate the effect of different geological parameters and interfacial parameters on the interaction mechanisms between HF and BPs. Gao and Ahmad (2020) utilized a two-dimensional finite element method (FEM) to specifically assess the effects of rock and bedding plane characteristics on height growth in layered unconventional reservoirs. Zhang et al. (2024) adopted a continuum-discontinuum element method (CDEM) to study the laws by which bedding planes, interlayer stress contrast, and modulus difference affect hydraulic fracture height growth. In addition, several studies have developed three-dimensional geological models with BPs based on specific reservoir conditions to analyze hydraulic fracture geometry under varying geological and engineering parameters, thereby providing practical guidance for field operations. For instance, Zou et al. (2017), Cong et al. (2022), Zhang et al. (2024), and Li et al. (2025) used discrete lattice methods to analyze the fracture morphology in multi-BPs formations under the influence of engineering parameters and bedding properties. Zhou et al. (2020) and Zhang et al. (2023) employed the discrete element method (DEM) to specifically address the ability of fracture to penetrate bedding planes under different combinations of engineering parameters. However, these studies have provided valuable insights into fracture height growth and HF–BP interaction. Nevertheless, they did not account for the thermo-hydro-mechanical coupling effects during the fracture propagation in formations containing BPs. The impact of thermal stress on fracture height evolution, as well as on interactions between hydraulic fractures and BPs, should not be overlooked, particularly in geothermal or deep reservoirs.

For simulating the hydraulic fracturing process with thermal effects, various thermo-hydro-mechanical (THM) models have been developed to simulate hydraulic fracturing processes. These models can be categorized by their theoretical frameworks into the following types: (1) thermo-hydro-mechanical-damage (THMD) models, which incorporate damage variables based on the FEM (Zhang et al., 2023); (2) extended finite element method (XFEM) (Zeng et al., 2020); (3) boundary element method (BEM) (Li and Zhang, 2023); (4) DEM (Jiao et al., 2021; Wang et al., 2024). Despite the considerable body of research in this area, studies specifically addressing the interaction between hydraulic fracture and natural weak planes remain relatively limited. Wang et al. (2022b) and Zhang et al. (2023) developed 2D geothermal reservoir models containing complex natural fracture networks using the THMD model to simulate fracture propagation and geothermal production behavior. Luo et al. (2022) employed a 2D THMD model to research the intersection of hydraulic fracture with natural fractures, indicating that thermal stress plays a positive role in activating natural fractures. Zhang et al. (2023) applied the two-dimensional THMD model to reveal that the incorporation of a thermal field reduces the fracture pressure and promotes fracture-network complexity.

In summary, most existing studies have not considered thermo–hydro–mechanical coupling during the hydraulic fracturing process. Among the limited studies that incorporate temperature effects, the research is predominantly based on two-dimensional models and mainly focuses on the influence of geological and engineering parameters on fracture morphology, while neglecting the evolution characteristics of BPs and lacking in-depth analysis of the interaction mechanisms between HF and BPs under thermal stress.

The FEM offers advantages in solid mechanics computations, while the DEM is more suitable for modeling fracture propagation in heterogeneous reservoirs or those containing natural weak planes. This work employs the CDEM, an explicit dynamic numerical approach that integrates both of the aforementioned methods. In recent years, a growing number of studies have applied CDEM to simulate three-dimensional fracture propagation under reservoir conditions without thermal effects (Zhu et al., 2021; Ren et al., 2022; Zhang et al., 2025).

The CDEM was used to develop a three-dimensional thermo-hydro-mechanical coupled hydraulic fracturing model (CDEM–THM). Numerical simulations of fracture propagation were conducted for deep shale reservoirs containing bedding planes, accompanied by a comprehensive analysis of the fracture height growth mechanisms and hydraulic fracture-bedding plane interaction behaviors under the combined effects of thermal stress (reservoir temperature and thermal expansion coefficient), vertical stress difference, and bedding plane cohesion. Compared with existing studies, this work reveals the evolution characteristics of fracture propagation behavior and bedding plane activation under the participation of thermal stress in a three-dimensional thermo–hydro–mechanical coupling framework, thereby addressing the shortcomings of previous studies in investigating the interaction mechanisms between HFs and BPs under thermal stress. The findings of this study provide a theoretical basis for forecasting fracture propagation morphology in field operations targeting deep shale reservoirs.

2. Mathematical model

Fig. 1 presents the fundamental principle of the CDEM. In this method, the rock matrix consists of blocks and interfaces. The blocks are composed of multiple solid elements, while the interfaces include both real interfaces (existing between blocks) and virtual interfaces (existing between solid elements). The real interfaces represent naturally occurring weak planes within the rock matrix, whereas the virtual interfaces indicate potential paths for matrix failure. Solid elements are interconnected via springs linking solid nodes, with spring failure representing the initiation

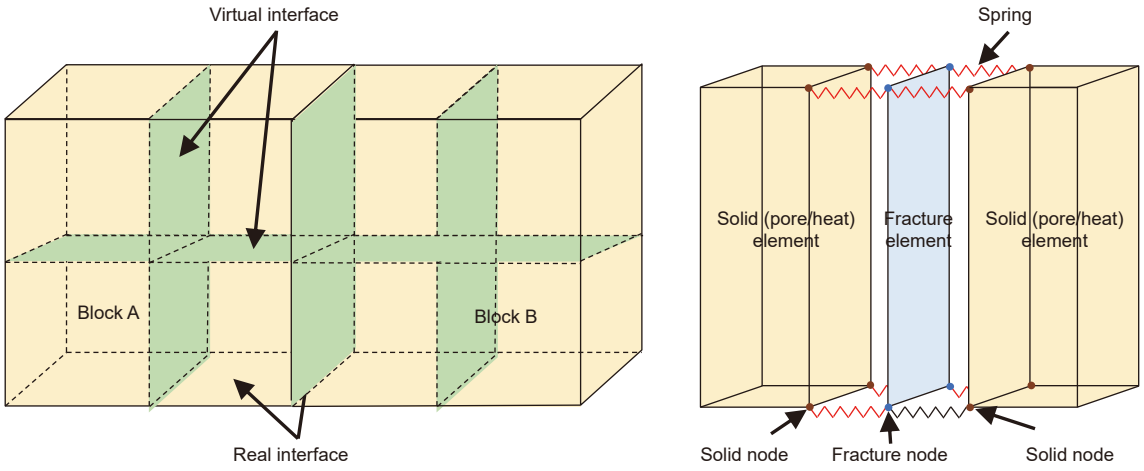


Fig. 1. Schematic diagram of the basic model in CDEM.

of fractures. In this study, pore flow and temperature field computations are performed using the same elements and nodes as those employed for the solid mechanical calculations. For fracture flow, the analysis is based on fracture elements and nodes embedded between the solid elements.

2.1. Solid field calculation model

The governing equations of the CDEM are formulated using a generalized Lagrangian approach. The dynamic equilibrium equation is expressed as follows (Ju et al., 2016):

$$\sigma_{ij,j} + f_i - \rho\ddot{u}_i - \mu\dot{u}_i = 0 \tag{1}$$

Due to the presence of stress partial derivative terms, this equation cannot be directly solved numerically. Using the variational principle, it can be reformulated into the fundamental dynamic equation:

$$\boldsymbol{M\ddot{u}} + \boldsymbol{C\dot{u}} + \boldsymbol{Ku} = \boldsymbol{F} \tag{2}$$

In Eqs. (1) and (2), $\sigma_{ij,j}$ is the divergence of the stress tensor, Pa·m^{-1}; f_i is external force, Pa·m^{-1}; ρ is rock density, kg·m^{-3}; u_i is displacement, m; $\boldsymbol{M}$ is element mass matrix, kg; $\boldsymbol{C}$ is element damping matrix, Pa; $\boldsymbol{K}$ is element stiffness matrix, kg·s^{-2}; $\boldsymbol{F}$ is node external force array, N; $\ddot{\boldsymbol{u}}$ is node acceleration array, m·s^{-2}; $\dot{\boldsymbol{u}}$ is node velocity array, m·s^{-1}; $\boldsymbol{u}$ is node displacement array, m.

For linearly elastic materials, the stress-strain relationship is described as follows (Guo et al., 2025):

$$\sigma_{ij} = 2G\varepsilon_{ij} + \left(K - \frac{2}{3}G\right)\theta\delta_{ij} \tag{3}$$

The model accounts for pore pressure and thermal stress through the following representations:

$$\sigma_{ij}' = \sigma_{ij} - \alpha_{\mathrm{p}} p_{\mathrm{m}} \delta_{ij} \tag{4}$$

$$\sigma_{\mathrm{T}} = \frac{E\alpha_{\mathrm{T}}(T - T_0)}{(1 - 2\nu)} \tag{5}$$

By combining Eqs. (3)–(5), the constitutive relation for the solid phase can be derived as follows:

$$\sigma_{\mathrm{e}ij} = 2G\varepsilon_{ij} + \left(K - \frac{2}{3}G\right)\theta\delta_{ij} - \alpha_{\mathrm{p}} p_{\mathrm{m}}\delta_{ij} - \frac{E\alpha_{\mathrm{T}}(T - T_0)}{(1 - 2\nu)} \tag{6}$$

where σ_{ij} is total stress tensor, Pa; σ_{ij}' is effective stress tensor, Pa; ε_{ij} is strain tensor; G is shear modulus, Pa; K is volume modulus, Pa; θ is volumetric strain; $\delta_{i,j}$ is Kronecker delta; α_{p} is pore pressure coefficient; p_{m} is pore pressure, Pa; σ_{T} is thermal stress, Pa; T is temperature, K; E is elasticity modulus, Pa; α_{T} is thermal expansion coefficient, K^{-1}; T_0 is reference temperature, K; ν is Poisson's ratio.

The nodal strains are determined from the geometric relationships.

$$\varepsilon_{ij} = \frac{u_{i,j} + u_{j,i}}{2} \tag{7}$$

where $u_{i,j}$ and $u_{j,i}$ are the first-order partial derivatives of displacement with respect to the coordinates.

Adjacent solid elements are interconnected via springs at nodes, which obey Hooke's law. The corresponding contact force is given by (Feng et al., 2019):

$$\begin{aligned} F_{\mathrm{n}} &= \frac{EA}{L}\Delta u_{\mathrm{n}} = K_{\mathrm{n}}\Delta u_{\mathrm{n}} \\ F_{\mathrm{s}} &= \frac{GA}{L}\Delta u_{\mathrm{s}} = K_{\mathrm{s}}\Delta u_{\mathrm{s}} \end{aligned} \tag{8}$$

where F_{n} and F_{s} represent the normal and tangential contact forces, N; Δu_{n} and Δu_{s} represent the normal and tangential displacements, m; K_{n} and K_{s} represent the normal and tangential stiffness, N·m^{-1}; A is area, m^2; L is interface equivalent thickness, m.

Spring failure corresponds to fracture initiation within the rock matrix. Tensile failure of springs is determined by the maximum tensile stress criterion, while shear failure is assessed using the Mohr-Coulomb criterion. The fracture criteria implemented in the model are as follows:

$$\begin{cases} \sigma_{\mathrm{n}} \geq \sigma_{\mathrm{t}} \\ \sigma_{\mathrm{s}} \geq c + \sigma_{\mathrm{n}} \tan\phi \end{cases} \tag{9}$$

The approach of abruptly reducing tensile strength and cohesion to zero upon failure does not accurately represent the residual strength still possessed by the rock mass after damage. Therefore, a fracture energy model is used for correction. The corrections for the contact force and strength after tensile failure and shear failure are shown in Eqs. (10) and (11), respectively.

$$\begin{cases} F_{\mathrm{n}}(t_{n+1}) = -\sigma_{\mathrm{t}}(t_n)A \\ \sigma_{\mathrm{t}}(t_{n+1}) = -\dfrac{\sigma_{\mathrm{t0}}^2 \Delta u_n(t_n)}{2G_{\mathrm{ft}}} + \sigma_{\mathrm{t}}(t_n) \end{cases} \tag{10}$$

$$\begin{cases} F_{\mathrm{s}}(t_{n+1}) = F_{\mathrm{n}}(t_{n+1})\tan\phi + c(t_n)A \\ c(t_{n+1}) = -\dfrac{c_0^2 \Delta u_{\mathrm{s}}(t_n)}{2G_{\mathrm{fs}}} + c(t_n) \end{cases} \tag{11}$$

where σ_{n} is tensile stress, Pa; σ_{s} is shear stress, Pa; σ_{t} is tensile strength, Pa; c is cohesion, Pa; ϕ is internal friction Angle, °; σ_{t0} is initial tensile strength, Pa; c_0 is initial cohesion, Pa; G_{ft} and G_{fs} represent the tensile and shear fracture energies, Pa·m; t is time, s;

Upon fracture initiation, the fracture width is calculated as the displacement difference of the solid nodes at both ends of the spring.

$$w = |(\boldsymbol{u}_1 - \boldsymbol{u}_2) \cdot \boldsymbol{n}_{12}| \tag{12}$$

where w is fracture width, m; $\boldsymbol{u}_1$, $\boldsymbol{u}_2$ represent nodal displacement at both ends of the spring, m; $\boldsymbol{n}_{12}$ is contact-surface normalized normal vector.

2.2. Seepage field calculation model

The presented model accounts for pore flow, fracture flow, and pore-fracture exchange. It is based on these assumptions: (1) the fluid is slightly compressible and the flow is single-phase; (2) pore flow follows Darcy's law; (3) fracture flow follows the cubic law. The corresponding continuity equation is given by:

$$C_{\mathrm{f}}\frac{\partial p}{\partial t} + \nabla\cdot\boldsymbol{v} = q \tag{13}$$

where C_{f} is fluid compression coefficient, Pa^{-1}; p is fluid pressure, Pa; $\boldsymbol{v}$ is fluid velocity vector, $\mathrm{m\cdot s^{-1}}$; q is source/sink term, $\mathrm{s^{-1}}$;

The fluid velocity in the pores is determined by Darcy's law, and is given by:

$$\boldsymbol{v} = -\frac{k}{\mu}k_{\mathrm{s}}\nabla p_{\mathrm{E}} \tag{14}$$

where k is permeability, $\mu\mathrm{m}^2$; μ is fluid viscosity, Pa·s; p_{E} is pressure on the pore nodes; k_{s} is relative permeability, which can be calculated as ${s_{\mathrm{a}}}^2(3-2s_{\mathrm{a}})$, where s_{a} is the average saturation of the pore element.

The flow velocity at pore nodes is given by (Zhu et al., 2021):

$$v_i = \frac{k_i}{\mu}k_{\mathrm{s}}\frac{1}{S}\sum_{j=1}^{M}\overline{p}_{\mathrm{E}j}n_{ij}L_j \tag{15}$$

where v_i is flow velocity on the pore nodes, $\mathrm{m\cdot s^{-1}}$; k_i is permeability in the i direction, $\mu\mathrm{m}^2$; S is pore element area, m^2; M is total number of edges on the pore element; $\overline{p}_{\mathrm{E}j}$ is average pressure on the j-th edge of the pore element, Pa; n_{ij} is the component of the unit normal vector of the j-th face in the i-direction; L_j is the j-th edge length.

From the above equations, the flow rate for pore element and the total rate at a pore node can be calculated.

$$q_{\mathrm{E}} = \sum_{j=1}^{M}\frac{\left(\boldsymbol{v}\cdot\boldsymbol{n}_j\right)S_j}{N_j} \tag{16}$$

$$Q_{\mathrm{E}} = \sum_{j=1}^{N_{\mathrm{E}}} q_{\mathrm{E}j} \tag{17}$$

where q_{E} is flow on the pore element, $\mathrm{m^3\cdot s^{-1}}$; $\boldsymbol{n}_j$ is the element normal vector on the j-th face; S_j is the total number of nodes on the j-th face of the pore element; N_j is the number of nodes on the j-th face; Q_{E} is total flow at a pore node, $\mathrm{m^3\cdot s^{-1}}$; N_{E} is the number of pore elements associated with this node.

The fluid pressure at a node can be determined from the following equation:

$$\Delta p_{\mathrm{E}} = -\frac{1}{C_{\mathrm{f}}}\frac{Q_{\mathrm{E}} + Q_e}{\phi V}\Delta t \tag{18}$$

The total fluid pressure at pore nodes is formulated as:

$$p_{\mathrm{E}}(t_1) = p_{\mathrm{E}}(t_0) + \Delta p_{\mathrm{E}} \tag{19}$$

where Q_e is external flow, $\mathrm{m^3\cdot s^{-1}}$; ϕ is porosity, and is regarded as 1 in the calculation of fracture flow; V is node volume, m^3.

The calculation procedure for fracture flow largely follows that for pore flow. Since fracture flow is implemented through fracture elements embedded between solid elements, which constitute a different set of elements and nodes from those used in pore flow, the equations require substitution of pore elements and pore nodes with fracture elements and fracture nodes. Consistent with the model assumptions that fluid flow in fractures follows the cubic law, the flow velocity at a fracture node can be calculated as (Zhang et al., 2024):

$$\boldsymbol{v} = -\frac{w^2}{12\mu}\nabla p_{\mathrm{f}} \tag{20}$$

where p_{f} is fracture node pressure, Pa.

Based on the average pressures in the pore elements and fracture elements, the flow exchange between pores and fractures can be calculated using Eq. (21), thereby achieving coupling between the two systems.

$$Q_{\mathrm{s}} = -\frac{k_E}{\mu}\frac{\overline{p}_{\mathrm{E}} - \overline{p}_{\mathrm{f}}}{d}A \tag{21}$$

where Q_{s} is flow rate between pore and fracture, $\mathrm{m^3\cdot s^{-1}}$; k_{E} is pore element permeability, $\mu\mathrm{m}^2$; d is distance from the center of the pore element to the fracture, m; A is contact area between the pore element and the fracture element, m^2.

2.3. Thermal field calculation model

The model simulates the temperature field by considering heat conduction between the cool fracturing fluid and the hot rock walls, in addition to heat convection within the fluid. The governing equation for the temperature field is given by:

$$(\rho C)_{\mathrm{eff}}\frac{\partial T_{\mathrm{r}}}{\partial t} = Q_{\mathrm{s}} + \nabla\cdot\left(\lambda_{\mathrm{eff}}\nabla T_{\mathrm{r}}\right) - \rho_{\mathrm{f}}C_{\mathrm{f}}\boldsymbol{v}\cdot\nabla T_{\mathrm{r}} \tag{22}$$

where $(\rho C)_{\mathrm{eff}}$ is effective volumetric heat capacity, $\mathrm{J\cdot m^{-3}\cdot K^{-1}}$; T_{r} is reservoir temperature, °C; Q_{s} is heat source, $\mathrm{W\cdot m^{-3}}$; λ_{eff} is effective thermal conductivity, $\mathrm{W\cdot m^{-1}\cdot K^{-1}}$; ρ_{f} is fluid density, $\mathrm{kg\cdot m^{-3}}$; C_{f} is specific heat capacity of fluids, $\mathrm{J\cdot kg^{-1}\cdot K^{-1}}$.

The heat conduction process is governed by Fourier's law, yielding the heat flux for an element as (Wang et al., 2024):

$$q_{Ti} = -\lambda_{\text{eff}}\left(\frac{1}{V_s}\sum_{j=1}^{N_1}\overline{T}_j S_j n_{ij}\right) \tag{23}$$

The total heat flow at nodes resulting from heat conduction is obtained as follows:

$$Q_t = \sum_{j=1}^{N_2}\frac{\left(\boldsymbol{q}_T\cdot\boldsymbol{n}_j\right)S_j}{N_j} \tag{24}$$

$$Q_c = \sum_{j=1}^{N_3} Q_{tj} \tag{25}$$

where $\boldsymbol{q}_T$ is element heat flux, W·m^{-2}; Q_t is node heat flow, W; Q_c is total node heat flow, W; V_s is volume of solid element, m^3; N_1, N_2, N_3 represent the total number of faces of the block element, the number of faces related to this node by the block element, and the number of elements related to this node respectively; $\overline{T}_j$ is average temperature on the j-th face of the block element, K.

The calculation of heat convection requires the seepage velocity obtained from Eq. (15), yielding the heat flow at nodes due to heat convection as:

$$Q_f = \sum_{j=1}^{N_3}\left(\frac{-V_s\rho_f C_f\boldsymbol{v}\cdot\nabla T_r}{N_n}\right) \tag{26}$$

where Q_f is heat flow generated by thermal convection at nodes, W; N_n is the number of nodes on the solid element.

In summary, the temperature change at a node is given by:

$$\Delta T_r = \frac{\left(Q_c + Q_f + Q_b\right)\Delta t}{(\rho C)_{\text{eff}}V} \tag{27}$$

where Q_b is heat flow boundaries, W.

3. Model solution and verification

3.1. Model solution

The CDEM does not rely on a global stiffness matrix for solution but employs the dynamic relaxation method. As an explicit solution approach, this method introduces damping to drive the system from an initially unbalanced state to equilibrium, thereby transforming static problems into dynamic ones. The specific computational procedure consists of the following steps:

(1) First, based on Eq. (2), the nodal unbalanced force is determined from the external and internal forces, together with the damping term at the current time step.
(2) The nodal acceleration is then computed from the unbalanced force.
(3) Subsequently, velocity and displacement for the next time step are updated through explicit iteration.
(4) Using the updated solid element information, fracture initiation is assessed, followed by computations of the seepage and temperature field.
(5) All nodes are fixed at their new positions, and the iteration proceeds until the termination criteria are satisfied.

The coupling relationships among the solid, seepage, and temperature fields in the simulation are illustrated in Fig. 2. The nodal displacements and element strains computed from the solid field model influence fracture flow and pore flow by modifying fracture widths and element porosities, respectively. In turn, the pore and fracture pressures obtained from the seepage field calculations act as external forces affecting the solid field. Flow transfer occurs between pores and fractures due to pressure gradients. The seepage velocity obtained from pore flow calculations is applied to the temperature field. The computed temperature change generates thermal stress, which is subsequently incorporated into the solid field calculation as an externally applied force.

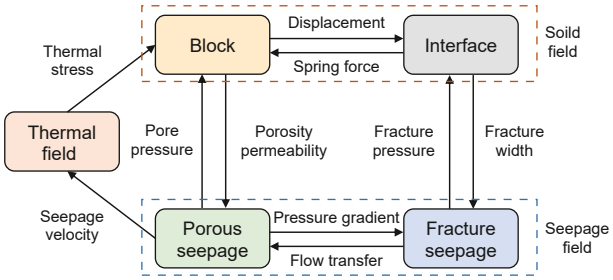


Fig. 2. Schematic diagram of the coupling relationship of the model.

3.2. Model validation

(1) Validation of heat transfer in a single fracture

The accuracy of the temperature field computation was validated against analytical solutions for single-fracture heat transfer (Lauwerier, 1955; Barends, 2010). The schematic diagram (Fig. 3) depicts a constant-width fracture bounded by hot rocks, with cool fluid entering from the injection point.

The analytical solution expresses the temperature T in terms of distance x and time t, with all parameters provided in Table 1.

$$T(x,t) = T_0 + (T_L - T_0)\operatorname{erfc}\left[\frac{(\lambda_s x)/\left(\rho_f C_f w\right)}{2\sqrt{\lambda_s/(\rho_s C_s)v_{in}(v_{in}t - x)}}\right]U(t - x/v_{in}) \tag{28}$$

where T_0 is rock temperature, °C; T_L is fluid temperature, °C; λ_s is rock thermal conductivity, W·m^{-1}·°C^{-1}; C_s is rock specific heat capacity, J·kg^{-1}·°C^{-1}; v_{in} is injection rate, m·s^{-1}; ρ_s is rock density, kg·m^{-3}; erfc is complementary error function.

Fig. 4 compares numerical and analytical solutions, showing temperature distribution along the x-direction across multiple time steps. The numerical solution agrees well with the analytical solution: the maximum discrepancy is 3.4%, and the temperature distribution at different times show close agreement, validating the accuracy of the temperature field computation.

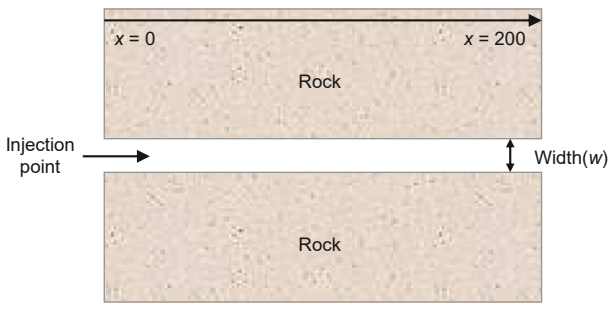


Fig. 3. Schematic diagram of single-fracture heat transfer.

Table 1
The parameters for the heat transfer model for single fracture flow.

Parameters	Values	Parameters	Values
Rock temperature, °C	200	Fluid temperature, °C	20
Rock thermal conductivity, $W{\cdot}m^{-1}{\cdot}°C^{-1}$	3	Specific heat capacity of rock, $J{\cdot}kg^{-1}{\cdot}°C^{-1}$	1000
Rock density, $kg{\cdot}m^{-3}$	2600	Fluid density, $kg{\cdot}m^{-3}$	1000
Specific heat capacity of fluid, $J{\cdot}kg^{-1}{\cdot}°C^{-1}$	4200	Injection rate, $m{\cdot}s^{-1}$	0.2
Fracture width, m	0.001		

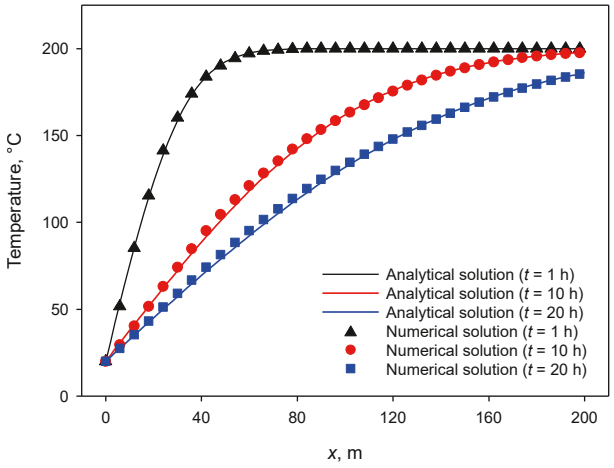


Fig. 4. The distribution of temperature along the x at different times.

(2) Validation of fracture propagation

For the fracture propagation process, validation was performed using the Penny-shaped fracture solution. The analytical solution was initially derived by Savitski and Detournay (2002), and later refined by Dontsov (2016) through an approximation of complex functions. This solution is widely adopted for verifying the accuracy of three-dimensional fracture propagation simulations. For both viscosity-dominated and toughness-dominated regimes in fracture propagation, Dontsov introduced the dimensionless time t_d and the fluid loss parameter ϕ_L. The dominant regime can be determined based on the values of $\log_{10}(t_d)$ and $\log_{10}(\phi_L)$, with the specific calculation method given by the following equations:

$$t_d = t\left(\frac{\mu'^5 E'^{13} Q^3}{K'^{18}}\right)^{-1/2} \quad \phi = \frac{\mu' E'^{11} C'^4 Q}{K'^{14}} \tag{29}$$

$$E' = \frac{E}{1-\nu^2} \quad K' = 4\left(\frac{2}{\pi}\right)^{\frac{1}{2}} K_{IC} \quad \mu' = 12\mu \quad C' = 2C_L \tag{30}$$

where Q is injection rate, $m^3{\cdot}s^{-1}$; K_{IC} is fracture toughness, $MPa{\cdot}m^{0.5}$; C_L is leak off coefficient, $m{\cdot}s^{-0.5}$.

Analytical solution of the viscosity-dominated regime:

$$w = 1.1901\left(\frac{\mu'^2 Q^3 t}{E'^2}\right)^{1/9} (1+\rho)^{0.487}(1-\rho)^{2/3}$$
$$R = 0.6944\left(\frac{Q^3 E' t^4}{\mu'}\right)^{1/9} \tag{31}$$

Analytical solution of the toughness-dominated regime:

$$w = 0.6537\left(\frac{K'^4 Q^3 t}{E'^4}\right)^{1/9}\left(1-\rho^2\right)^{1/2}$$
$$R = 0.8546\left(\frac{E' Q t}{K'}\right)^{2/5} \tag{32}$$

where w is fracture width, m; R is half fracture length, m; ρ is normalized distance.

The verification model is illustrated in Fig. 5. It has dimensions of 120 ×120 × 40 m, and no in-situ stress is applied. A potential fracture plane is positioned at a depth of z = 20 m, with the injection point located at the center of model. The corresponding mesh layout is presented in Fig. 5. A hexagonal grid is adopted, with a cell size of 2 m along the fracture plane and 2 m in the longitudinal direction.

To better validate the accuracy of fracture propagation, two distinct cases were established and compared against their respective analytical solutions.

Case 1: E = 30 GPa, ν = 0.25, Q = 0.05 $m^3{\cdot}s^{-1}$, K_{IC} = 0.4 $MPa{\cdot}m^{0.5}$, μ = 2 mPa·s, C_L = 1 × 10^{-7}, t = 100 s. Under these parameters, $\log_{10}(t_d)$ = −3.55, $\log_{10}(\phi_L)$ = −9.29, the fracture is viscosity-dominated. The corresponding fracture morphology is depicted in Fig. 6(a). Fig. 7 compares the numerical and M-analytical solutions, depicting the evolution of fracture length and width over time. For the viscosity-dominated case, the average error in fracture length is 2.8%, and 2.0% in fracture width. The overall minor discrepancies and close agreement with the analytical solution.

Case 2: By adjusting the tensile strength, K_{IC} was set to 5.6 $MPa{\cdot}m^{0.5}$ while keeping all other parameters identical to Case 1. Under these conditions, $\log_{10}(t_d)$ = 7.03 and $\log_{10}(\phi_L)$ = −25.76, indicating a toughness-dominated fracture propagation regime. The resulting fracture morphology is presented in Fig. 6(b). Fig. 8 presents the comparison with K-analytical solution. For this toughness-dominated case, the model achieves average errors of only 2.5% in fracture length and 2.2% in width.

In summary, the results from Case 1 and Case 2 collectively demonstrate the accuracy of the proposed model in simulating three-dimensional fracture propagation.

(3) Validation of hydraulic fracture-natural weak planes interaction behaviors

To validate the accuracy of the model in simulating interactions between HF and natural weak planes, the simulation results were compared with experimental data from true triaxial hydraulic fracturing tests on natural fractures with varying approach angles (Gu et al., 2012), as the study involves the intersection behavior between HFs and BPs.

The model parameters were set consistently with the experimental conditions. The simulation results are shown in Fig. 9, and a comparison between the simulation and experimental results is presented in Table 2. Gu's experimental (Gu et al., 2012) results are categorized into two cases: crossing and no crossing, and the simulation results correspond precisely to the experimental outcomes.

4. Model establishment of a deep shale reservoir with bedding planes

Fig. 10 shows a deep laminated shale reservoir model was constructed for numerical simulation studies. The model dimensions are 80 m × 60 m × 60 m, with bedding planes positioned at z = 20 m and z = 40 m. To account for the

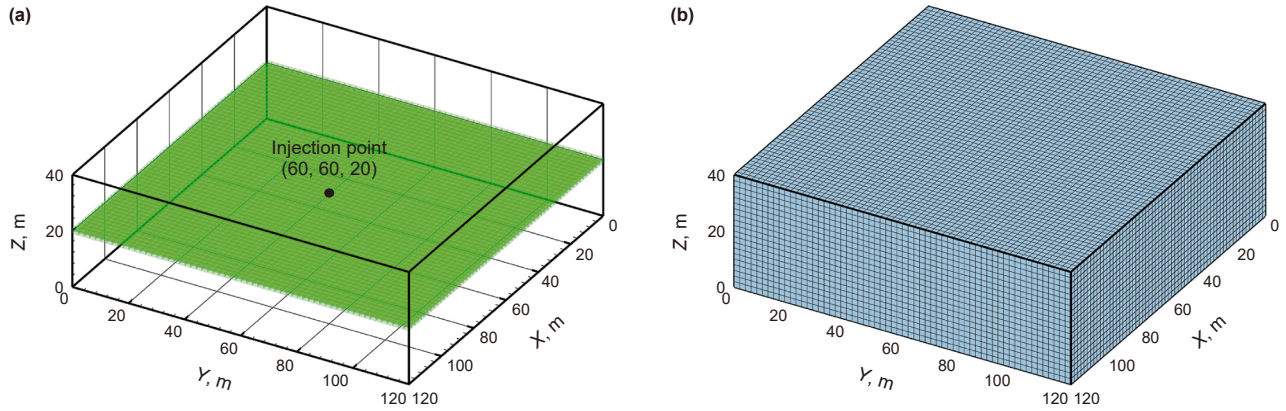


Fig. 5. The fracture propagation model used for verification with Penny model.

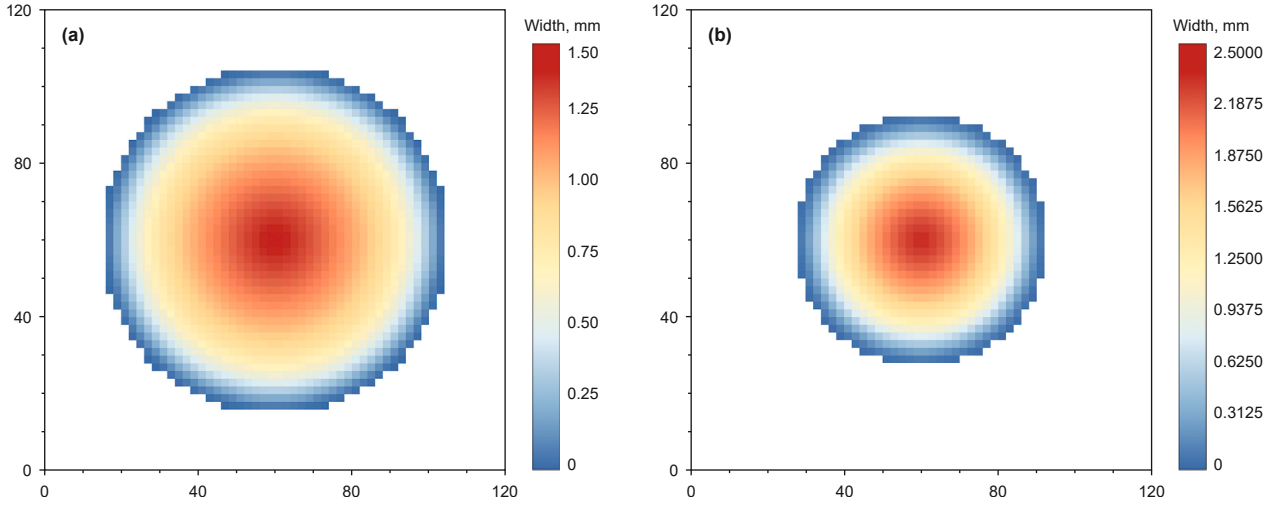


Fig. 6. The fracture morphology of the numerical solution: (**a**) viscosity-dominated fracture; (**b**) toughness-dominated fracture.

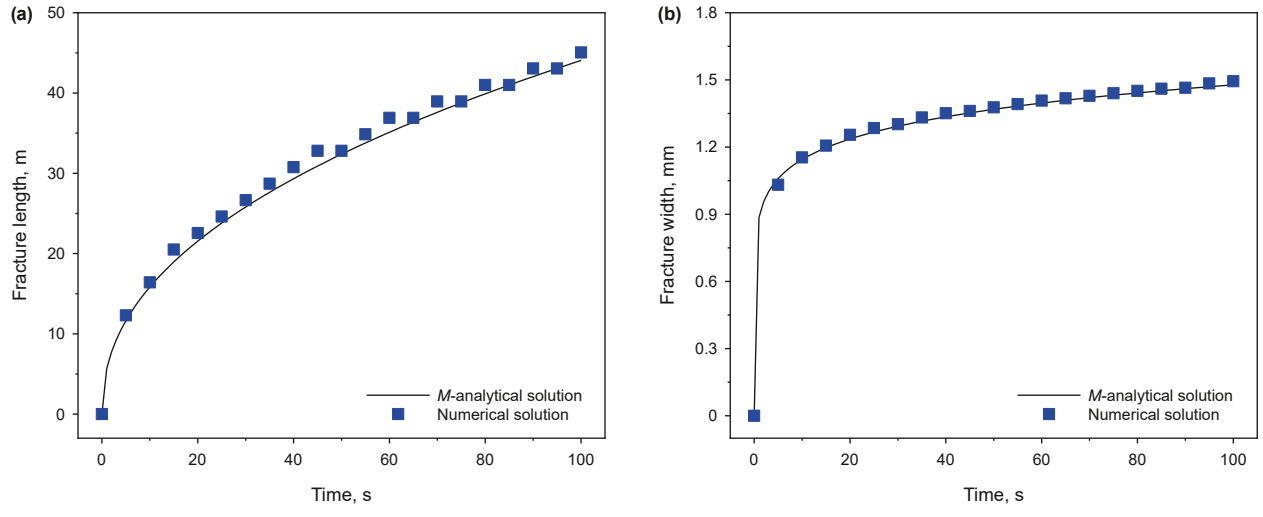


Fig. 7. Comparison of numerical solution and *M*-analytical solution: (**a**) fracture length; (**b**) fracture width.

distinct mechanical properties of shale reservoirs along directions parallel and perpendicular to the bedding planes, the reservoir was modeled as a transversely isotropic material. A 2.5 m hexahedral mesh was adopted, with the mesh size selected based on a balance between computational accuracy and efficiency.

The boundary conditions of the model are specified as follows. For the stress field, normal displacement constraints are applied at

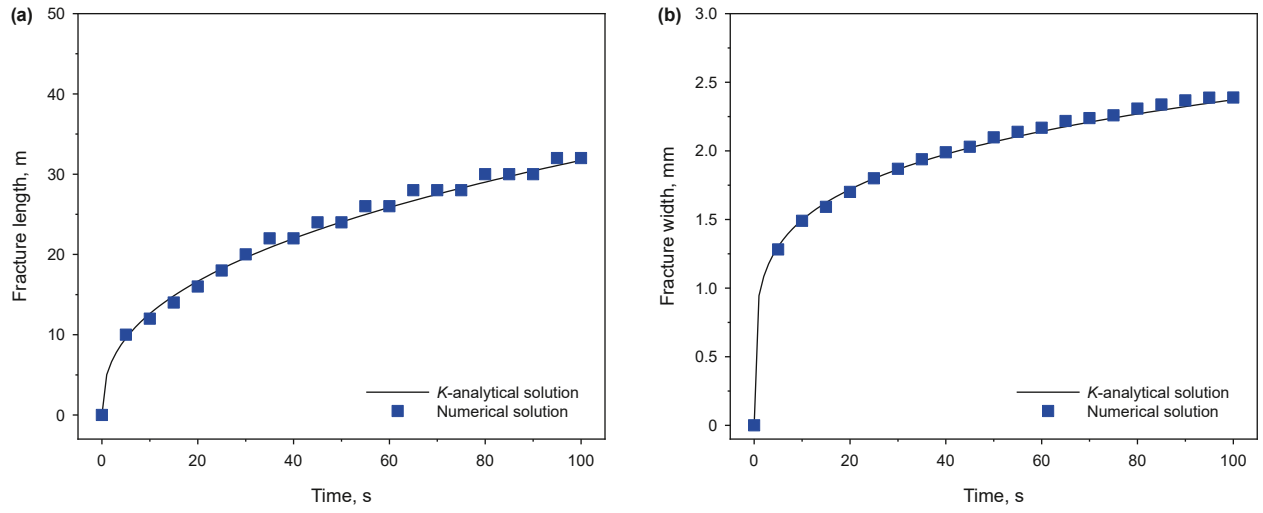


Fig. 8. Comparison of numerical solution and *K*-analytical solution: (**a**) fracture length; (**b**) fracture width.

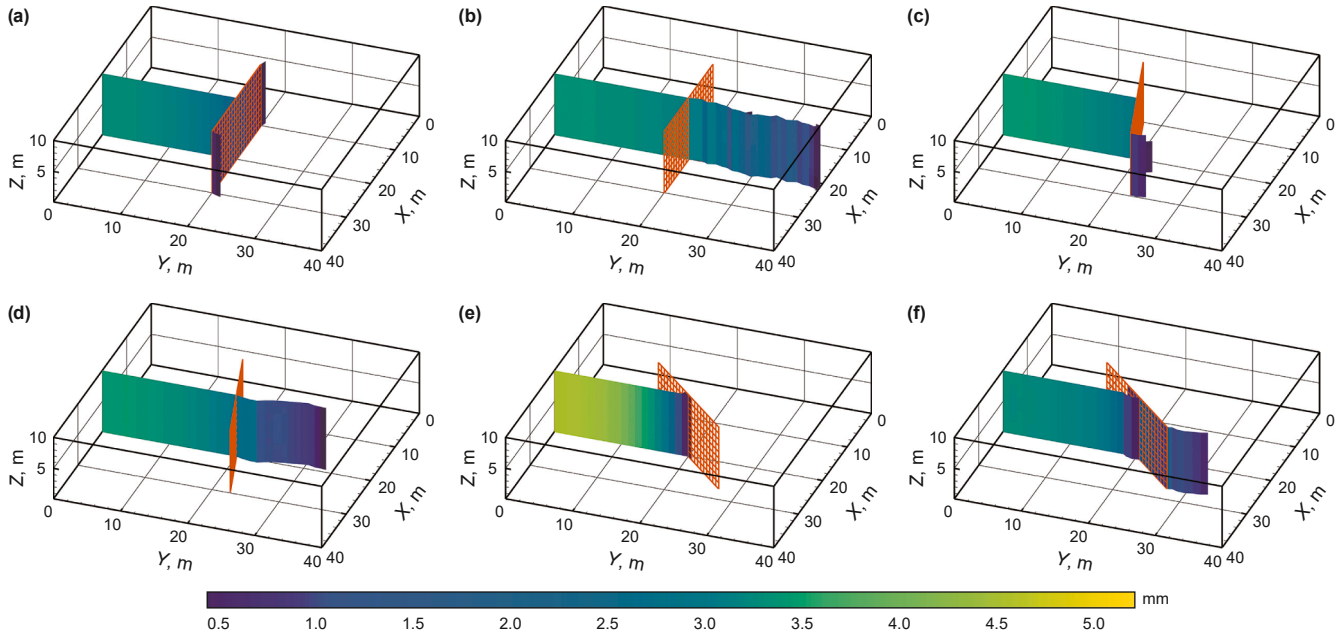


Fig. 9. Simulation results of the intersection of HF with individual NF: (**a**) 90°, 7.58 MPa; (**b**) 90°, 13.79 MPa; (**c**) 75°, 8.27 MPa; (**d**) 75°, 17.24 MPa; (**e**) 45°, 8.27 MPa; (**f**) 45°, 17.24 MPa.

Table 2
Comparison of simulation results with Gu's experimental results.

Case	NF parameters	Approach angle, °	$\sigma_{H,}$ MPa	$\sigma_{h,}$ MPa	Experimental	Simulation
1	Cohesion:	90	7.58	6.89	No crossing	No crossing
2	0 MPa	90	13.79	6.89	Crossing	Crossing
3	Friction	75	8.27	6.89	No crossing	No crossing
4	coefficient:	75	17.24	6.89	Crossing	Crossing
5	0.615	45	8.27	6.89	No crossing	No crossing
6		45	17.24	6.89	No crossing	No crossing

the model boundaries, and the minimum horizontal principal stress (σ_h), maximum horizontal principal stress (σ_H), and vertical stress (σ_v) are applied in the *X*, *Y*, and *Z* directions, respectively, to establish the in-situ stress state. For the fluid field, the injection point is located at the center of the model (40, 30, 30), and a constant injection rate is applied. The model boundaries are set as open boundaries, and the pumping duration is 1080 s. For the temperature field, the initial reservoir temperature ranges from 20 to 300 °C, and the injection fluid temperature is set to 20 °C. The outer boundaries of the model are treated as adiabatic boundaries. Reservoir parameters settings are based on data from actual deep shale reservoirs, as listed in Table 3.

5. Results and analysis

5.1. The effect of thermal stress

The temperature difference between the reservoir and injected fluid, along with the formation's thermal expansion coefficient

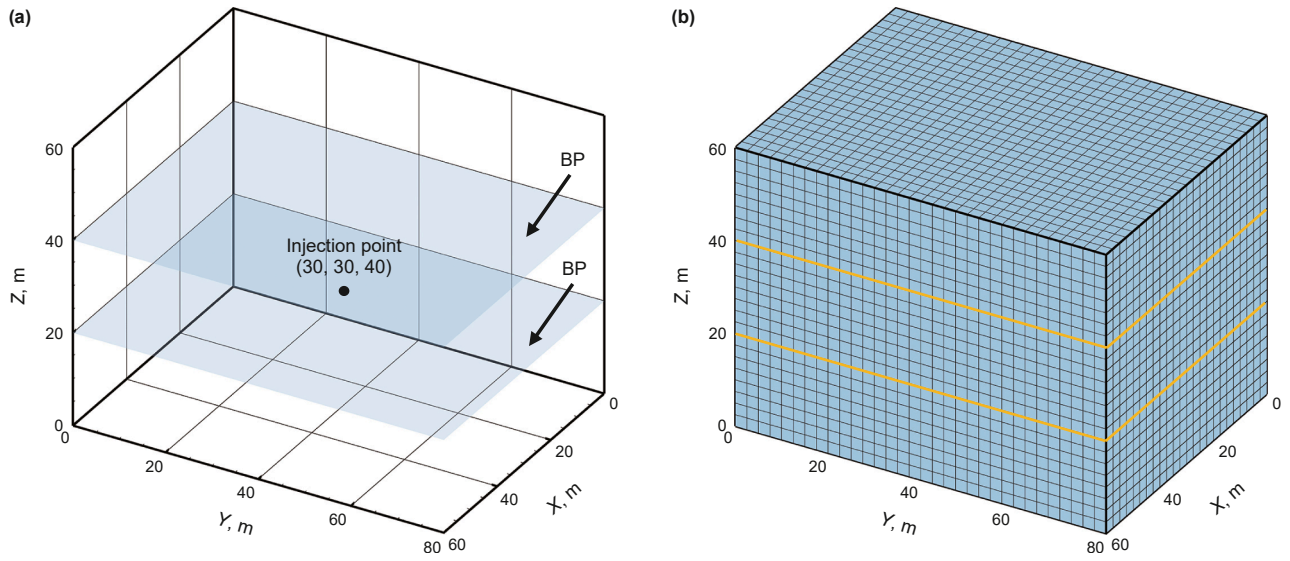


Fig. 10. The model of deep shale reservoir with bedding planes.

Table 3
Parameters of the fracture propagation model.

Categories	Parameters	Values
Rock matrix	Poisson's ratio	0.26 (Horizontal)/0.2 (Vertical)
	Elastic modulus	40 (Horizontal)/30 (Vertical) GPa
	Temperature	200 °C
	Permeability	1×10^{-17} m^2
	Pore pressure	70 MPa
	Tensile strength	6 MPa
	Cohesion	20 MPa
	Friction angle	40°
	Fracture energy	100 (Normal)/500 (Tangential) Pa·m
	Coefficient of heat conduction	2.5 W·m^{-1}·°C^{-1}
	Specific heat capacity	950 J kg^{-1}·°C^{-1}
	Coefficient of thermal expansion	10×10^{-6} °C^{-1}
	In-situ stress ($\sigma_H/\sigma_h/\sigma_v$)	102/90/96 MPa
Operation parameters	Injection rate	1.5 m^3·min^{-1}
	Viscosity	2.5 mPa·s
	Temperature	20 °C
	Coefficient of heat conduction	0.59 W·m^{-1}·°C^{-1}
	Specific heat capacity	4200 J·kg^{-1}·°C^{-1}
	Coefficient of thermal expansion	2.5×10^{-4} °C^{-1}
Bedding planes	Tensile strength	1 MPa
	Cohesion	2.5 MPa
	Friction angle	10°
	Fracture energy	10 (Normal)/50 (Tangential) Pa·m

(α_T), are the primary parameters influencing thermal stress. This section explores the mechanisms by which thermal stress affects fracture height growth and the interaction between HF and BP, based on simulation results under varying formation temperatures (20 °C—representing the same temperature as the injected fluid, thus no thermal stress, as well as 100, 200, and 300 °C) and thermal expansion coefficients (5×10^{-6}, 10×10^{-6}, and 15×10^{-6} °C^{-1}). The other parameters remain consistent with those in Table 3. Fig. 11 illustrates the fracture morphologies under different thermal expansion coefficients and temperatures.

5.1.1. The influence mechanism of thermal stress on hydraulic fracture

Fig. 11(a) shows the case at 20 °C, where thermal stress is not considered. Under the reservoir conditions specified in Table 3, the HF directly crosses the BPs. At the α_T of 5×10^{-6} °C^{-1}, Fig. 11(b)–(d) present the fracture morphology at different temperatures. Compared with the 20 °C case, the fracture length is slightly shorter and the fracture width is slightly larger at 100 °C and 200 °C, although the overall changes remain modest. At 300 °C, the HF induces minor secondary fractures at the BPs. Fig. 11(e)–(g) present the results for the α_T of 10×10^{-6} °C^{-1}. The HF maintains its the crossing behavior without activating the BPs at 100 °C. When the temperature increases to 200 °C, transverse secondary fractures emerge near the injection point. While the HF continues to cross the BPs, it experiences minor activation, though its extent remains limited. At 300 °C, more pronounced secondary fractures develop perpendicular to the main fracture, with evident opening of the BPs. Despite this, the HF still achieves crossing through BPs. Fig. 11(h)–(j) display the results for an increased α_T of 15×10^{-6} °C^{-1}. The fracture morphology shows moderately larger fracture width compared to Fig. 11(b) and (e) at 100 °C, the overall geometry remains similar. At 200 °C, HF crosses BPs accompanied by the initiation of secondary fractures, and the BPs become clearly activated. When the temperature reaches 300 °C, numerous secondary fractures develop along the sides of the HF. Concurrently with this development, both its height and length are significantly reduced. Under these conditions, the HF fails to cross the BPs. This phenomenon occurs because all simulation cases were run for the same time duration, implying an equal injected fluid volume. The formation of numerous secondary fractures consumed a substantial portion of the injected fluid; with continued injection, the BPs would eventually be crossed.

Fig. 12 illustrates the temporal evolution of the HF parameters under different thermal expansion coefficients and temperatures. As shown in Fig. 12, with α_T of 10×10^{-6} °C^{-1}, elevating the temperature from 100 °C to 300 °C results in reduced fracture dimensions: height decreases by 14.3% (from 35 to 30 m) and the width at the injection point exhibits a marked 27.6% increase, reaching 5.32 mm from an initial 4.17 mm. At 200 °C, as α_T increases from 5×10^{-6} °C^{-1} to 15×10^{-6} °C^{-1}, both fracture height and length decrease from 35 m to 30 m, representing a 14.3%

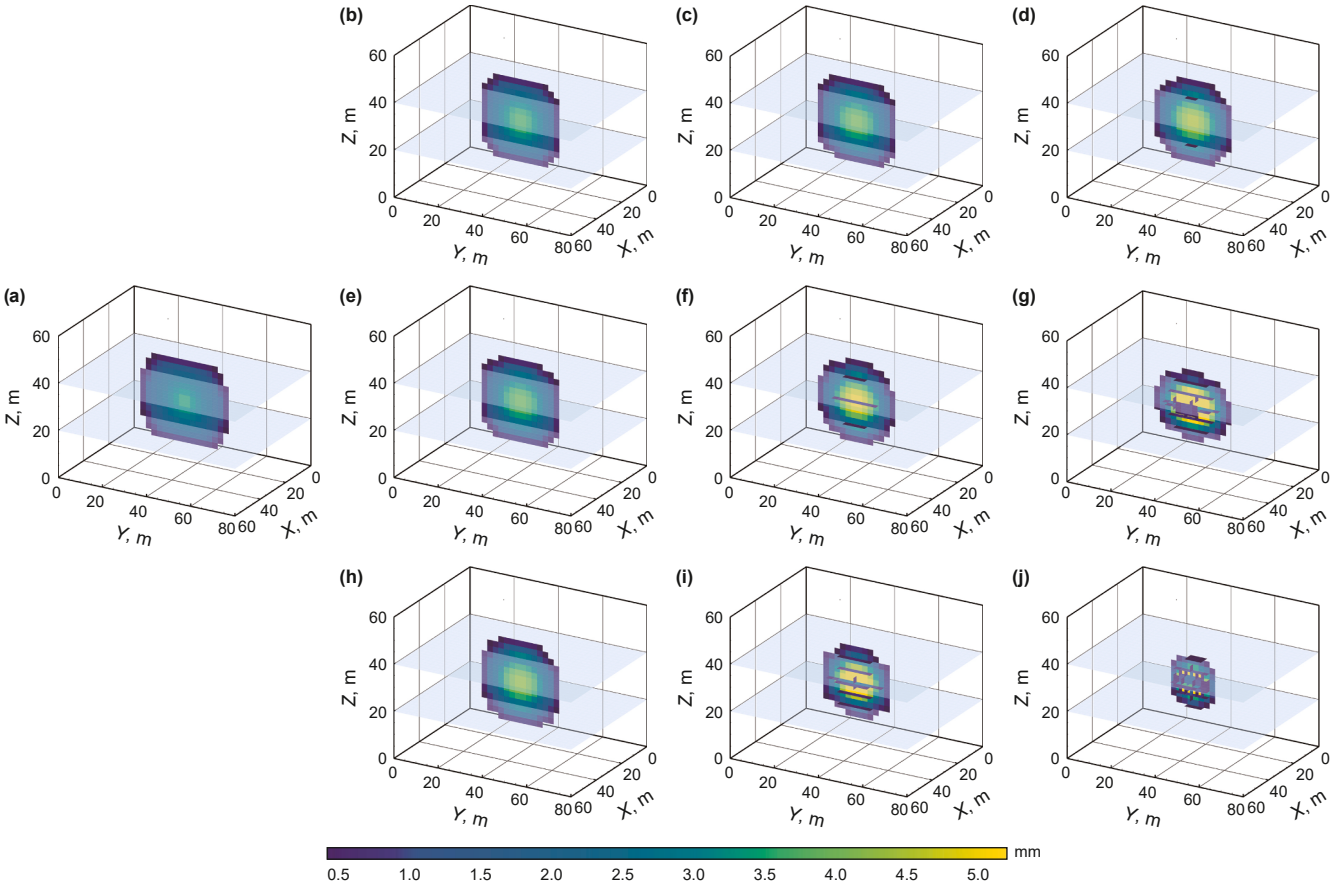


Fig. 11. Fracture width distributions under different reservoir thermal expansion coefficients and formation temperatures: (**a**) 20 °C (no thermal stress); (**b**) 5×10^{-6} °C^{-1}, 100 °C; (**c**) 5×10^{-6} °C^{-1}, 200 °C; (**d**) 5×10^{-6} °C^{-1}, 300 °C; (**e**) 10×10^{-6} °C^{-1}, 100 °C; (**f**) 10×10^{-6} °C^{-1}, 200 °C; (**g**) 10×10^{-6} °C^{-1}, 300 °C; (**h**) 15×10^{-6} °C^{-1}, 100 °C; (**i**) 15×10^{-6} °C^{-1}, 200 °C; (**j**) 15×10^{-6} °C^{-1}, 300 °C.

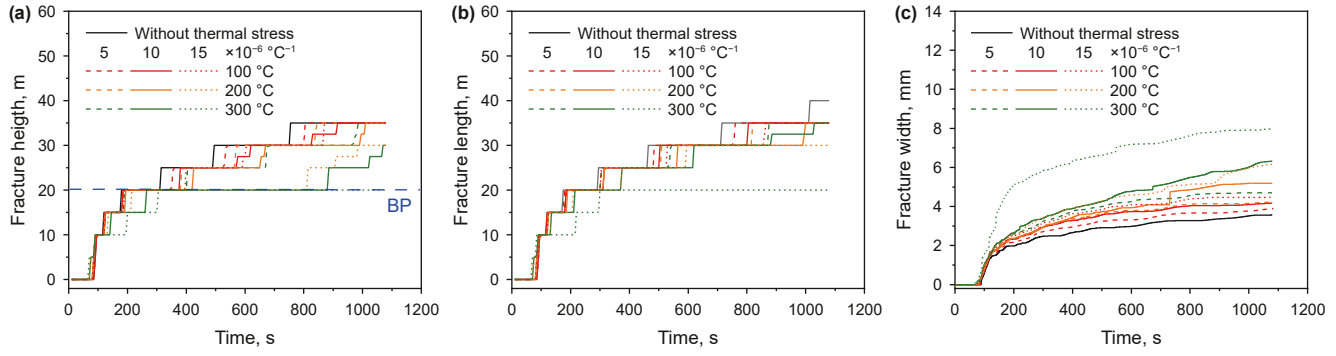


Fig. 12. The temporal evolution of HF parameters under different reservoir thermal expansion coefficients and temperatures: (**a**) HF height; (**b**) HF length; (**c**) injection point width.

reduction for each. Conversely, the injection point width expands from 4.23 mm to 6.15 mm, indicating a 45.4% increase. As reservoir temperature and α_T increase, thermal stress intensifies, leading to a significant widening of fractures at the injection point. And the HF requires a longer time to reach a given height or length. Overall, this demonstrates a trend where higher reservoir temperature and α_T result in reduced fracture height and length. This is primarily because elevated temperatures increase fracture width, inevitably shortening the fracture height and length for the same fluid volume. Simultaneously, the activation of more BPs and the generation of additional secondary fractures dissipate a portion of the energy available for fracture propagation.

This section first examines how thermal stress influences HF characteristics. Since the effects of both α_T and temperature on simulation results originate from changes in the magnitude of thermal stress, their impacts exhibit similar trends, as can be observed from Fig. 11. Therefore, the analysis is based on four simulation cases presented in Fig. 11(a) and (e)–(g), in which α_T is

fixed at 10 × 10^{-6} °C^{-1} while the reservoir temperature varies. First, the temperature fields of cases shown in Fig. 11(e), (f), (g) are presented using slices along the main fracture, as illustrated in Fig. 13. Under different reservoir temperature conditions, the temperature variation is mainly concentrated within the fracture and its surrounding region and decays rapidly with distance.

To more intuitively illustrate the influence of thermal stress, the average normal stress along two monitoring lines was analyzed: line L1 from (0, 40, 30) to (60, 40, 30), which is perpendicular to the HF propagation direction, and line L2 from (30, 0, 30) to (30, 80, 30), which is aligned with the HF propagation direction, as presented in Fig. 14. The average normal stress is defined as the mean of the three in-situ principal stresses, adopting the convention that tensile stress is positive and compressive stress is negative.

The rapid cooling of rock from low-temperature fluid injection induces thermal stress, which acts as tensile stress on the fracture surfaces, a phenomenon clearly captured in Fig. 14(a). When thermal stress is not considered, the fluid pressure within the fracture exerts compressive stress on both sides of the fracture. As a result, the stress curve shows a gradual rise from the fracture region toward the far field. In contrast, when thermal stress is present, it acts as tensile stress, creating a low-stress zone near the fracture. On the curve, this is reflected as an initial drop followed by a rise. As the temperature rises, the magnitude of thermal stress increases, and this effect becomes more pronounced, substantially reducing the in-situ stress near the injection point. These findings explain why the fracture width increases significantly with increasing reservoir temperature and α_T. As presented in Fig. 14(b), when thermal stress is not considered, the fluid pressure decreases from the injection point toward the fracture tip, leading to a gradual reduction in compressive loading on the surrounding rock, and consequently the stress curve rises progressively. It then drops near the fracture tip due to stress concentration, before returning to its initial state after leaving the fracture region. When temperature is included, thermal stress significantly reduces the in-situ stress. The stress curve first rises from the injection point along the fracture because, although fluid pressure gradually decreases, the influence of thermal stress remains strong. Subsequently, the curve declines as the heat exchange of the cool fracturing fluid cannot keep pace with the fracture propagation, causing the thermal stress to weaken. This variation becomes increasingly pronounced with rising temperature.

Fig. 15 presents the fracture pressure and the three in-situ principal stresses at the injection point under different temperatures. The presence of thermal stress reduces the original in-situ stresses and decreases the difficulty of fracture initiation, thereby lowering the fracture pressure. At 200 °C, the fracture pressure is 4.33 MPa lower than that at 20 °C. Fig. 15(b) more intuitively demonstrates the influence of thermal stress on the three in-situ principal stresses. When comparing the 200 °C case with the 20 °C case, σ_h, σ_H, and σ_v decrease by 0.79 MPa, 4.53 MPa, and 3.95 MPa, respectively. Among these, σ_h shows the smallest reduction, while both σ_H and σ_v exhibit significant decreases. This indicates that thermal stress mainly reduces the principal stresses acting parallel to the fracture plane, resulting in tensile stress

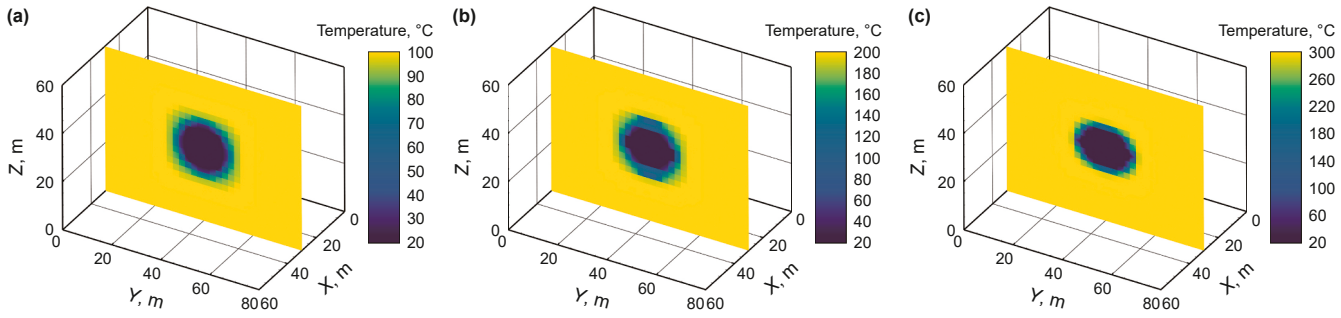


Fig. 13. Distribution of temperature field under different temperatures at the α_T of 10 × 10^{-6} °C^{-1}: (**a**) 100 °C; (**b**) 200 °C; (**c**) 300 °C.

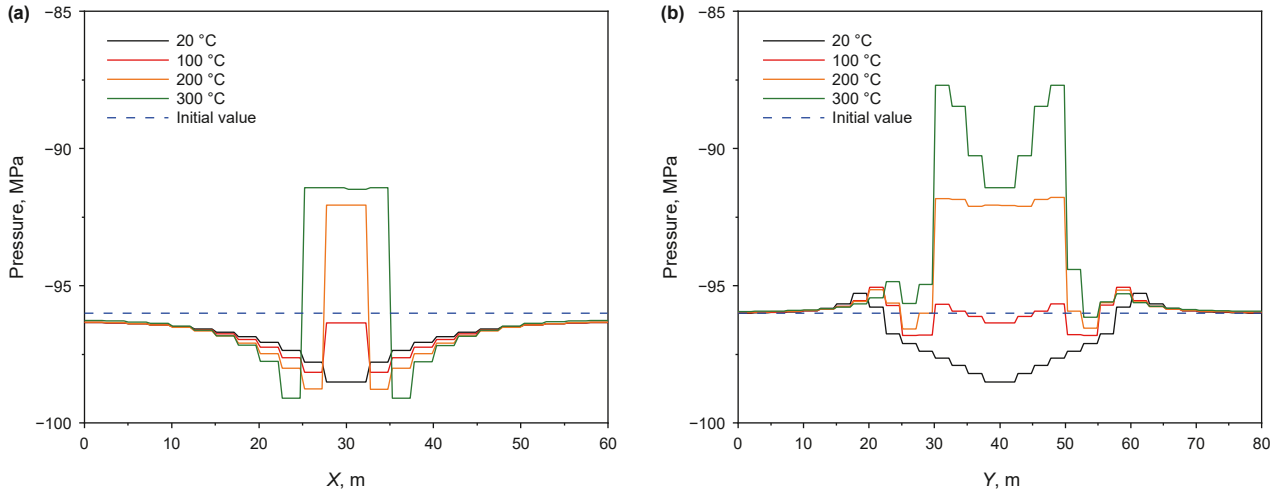


Fig. 14. Distribution of average normal stress under different temperatures at the α_T of 10 × 10^{-6} °C^{-1}: (**a**) perpendicular to the HF direction; (**b**) along the HF propagation direction.

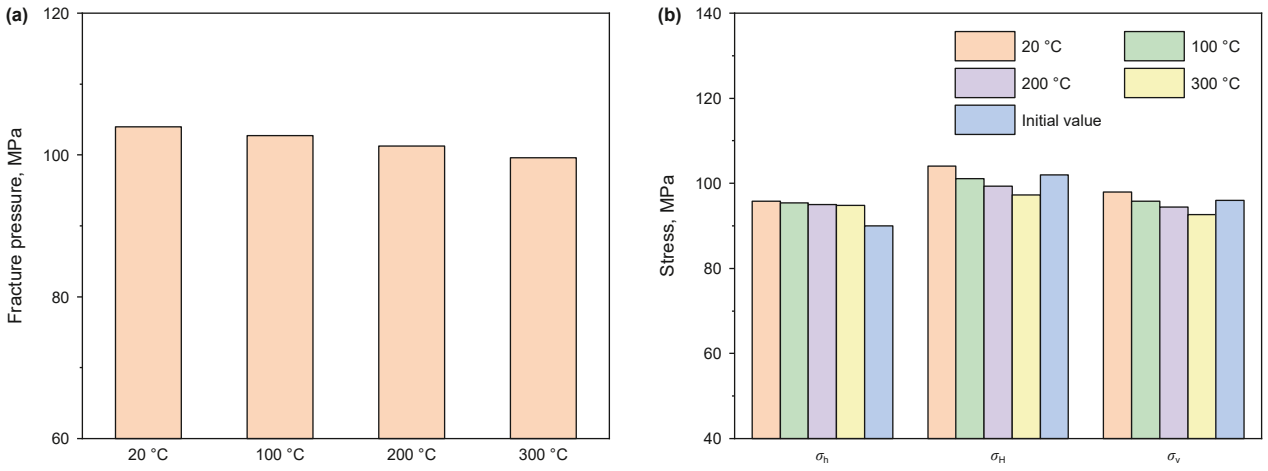


Fig. 15. Fracture pressure and three principal in-situ stresses at the injection point under different temperatures with the α_T of 10×10^{-6} °C^{-1}: (**a**) fracture pressure; (**b**) three in-situ principal stresses.

along the HF. Consequently, secondary fractures perpendicular to the HF plane trend to emerge with increasing thermal stress.

5.1.2. The influence mechanism of thermal stress on BPs

The effect of thermal stress on BPs is examined using the four simulation cases shown in Fig. 11(a), (e)–(g), in which the α_T is fixed at 10×10^{-6} °C^{-1} and the reservoir temperature is varied. The opening width and pressure distribution in the *x*-direction on the BPs were extracted along line L3 from (0, 40, 40) to (60, 40, 40), together with the temporal evolution of the activated bedding area, as presented in Fig. 16. Fig. 16(a) illustrates that at 200 °C the BP becomes activated, reaching an area of 143.75 m^2. At 300 °C, the activated region further expands to 250 m^2. Fig. 16(b) shows that compared with 200 °C, the maximum opening at 300 °C increases from 0.42 mm to 0.92 mm, and the opening range expands from 3.76 m to 4.77 m, indicating an overall increase. This is attributed to the higher thermal stress further reducing the resistance to BP opening, enabling more extensive activation. According to Fig. 16(c), at 20 °C and 100 °C the BP is directly crossed by the HF, producing a distinct peak in the fluid pressure along the *x*-direction of the BP at the crossing location. At temperatures of 200 °C and above, the interaction between the HF and the BPs shifts from a tip-like form to a plateau, indicating partial activation. With further temperature increase, the pressure at this plateau decreases, which is due to the greater thermal stress further reducing the normal stress at the BPs, thereby lowering the fluid pressure required to open them. Additionally, as the BPs is more extensively activated, the pressure influence range also increases to some extent.

To further analyze the mechanism by which thermal stress influences the BP, the normal stress distribution above the BP was extracted along line L4 (0, 40, 40) – (60, 40, 40) at 300 s, as shown in Fig. 17. At this moment, the fracture height in all four simulation cases has extended to the BPs. As the temperature rises, the normal stress on the BP progressively decreases. With continued simulation time, heat exchange becomes more adequate, further intensifying the reduction in normal stress. To open the BP in tension, the fluid pressure must overcome both the normal stress and BP's tensile strength. Therefore, the reduction in normal stress evidently lowers the difficulty of BPs opening, enabling HF to cross and partially activate the BPs at higher reservoir temperatures. Consequently, in reservoirs with higher temperatures and α_T, the induced thermal stress plays a positive role in activating BPs and natural fractures. Coupled with the generation of secondary fractures, this is conducive to the formation of more complex fracture networks.

Furthermore, due to differences in fracture propagation rates under different temperature conditions, the time at which the fracture reaches the bedding plane is not identical for each case, as shown in Fig. 12. Therefore, at this time, the duration of thermal stress acting near the bedding plane differs among the cases. However, as shown in Fig. 17, the stress-affected range observed along this path is generally similar under different temperature conditions and is mainly concentrated within the fracture–

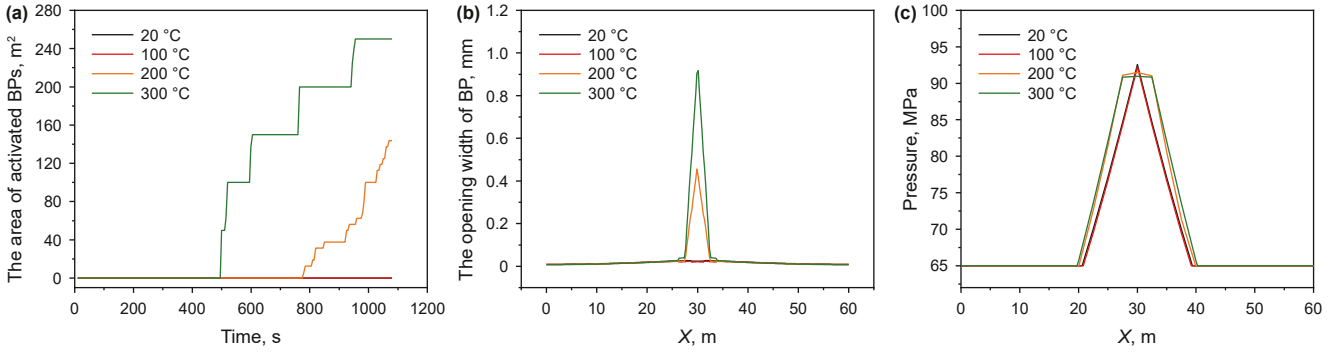


Fig. 16. The BP characteristics under different temperatures with the α_T of 10×10^{-6} °C^{-1}: (**a**) activated area, (**b**) bedding plane opening width along line L3, (**c**) fluid pressure along line L3.

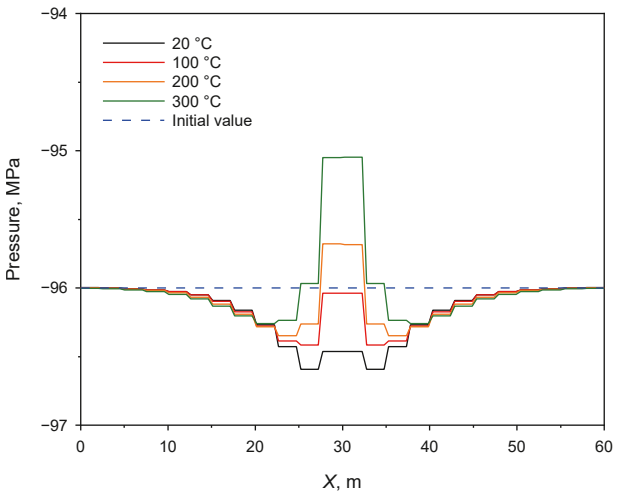


Fig. 17. Normal stress distribution along line L4 at 300 s under different temperatures with the α_T of 10×10^{-6} °C^{-1}.

bedding interaction region, without a noticeable expansion with increasing temperature or acting time. This indicates that although heat conduction continues to occur, its spatial propagation capability is limited and cannot significantly expand the affected region over time. In other words, the heat conduction rate does not govern the expansion of the stress-affected range, and its influence is mainly confined to the fracture and its vicinity.

5.2. The combined effect of vertical stress difference and thermal stress

The vertical stress difference (σ_v−σ_h) is a primary control on hydraulic fracture-bedding plane interactions. Based on simulations performed for (σ_v−σ_h) of 2, 6, and 12 MPa and formation temperatures of 20, 100, 200, and 300 °C, this section elucidates the coupled roles of thermal stress and vertical stress difference in governing fracture height evolution and fracture-bedding interactions. The remaining parameters are unaltered from Table 3. Fig. 18 compares the fracture morphologies for different vertical stress differences and formation temperatures.

The previous section analyzed the case with ($\sigma_v - \sigma_h$) = 6 MPa. Thermal stress promotes BP activation by reducing the compressive normal stress acting on the interface. As thermal stress increases, the interaction mode gradually changes from crossing to crossing with partial activation. In this section, we focus on the cases at ($\sigma_v - \sigma_h$) of 2 MPa and 12 MPa.

When ($\sigma_v - \sigma_h$) increases to 12 MPa, the higher normal confinement suppresses BP activation, promoting direct fracture crossing. As shown in Fig. 18(i)–(l), within the current simulation range, the HFs all cross the BPs without activating them. However, at 300 °C, secondary fractures appear near the injection point. Although the BPs are not activated, the way thermal stress influences the BPs is consistent with the ($\sigma_v - \sigma_h$) = 6 MPa case: thermal stress lowers the normal stress across the interface, thereby reducing the difficulty of activation. Under higher vertical stress, a higher thermal stress was required to achieve the activation effect. Therefore, a large vertical stress difference weakens the influence of thermal stress on BP activation. Fig. 19 depicts the temporal evolution of HF parameters. The overall trend is consistent with that seen at ($\sigma_v - \sigma_h$) of 6 MPa. Within a simulation time of 1080 s, increasing the temperature from 20 °C to 300 °C reduces the fracture height from 35 m to 32.5 m (by 7.1%) and the fracture length from 40 m to 30 m (by 25%), while increasing the injection-point fracture width from 3.57 mm to 6.56 mm (by 83.8%).

With ($\sigma_v - \sigma_h$) of 2 MPa, the lower vertical stress causes the HF to be more inclined to extend along the BP. This condition differs from those with ($\sigma_v - \sigma_h$) of 6 and 12 MPa. Fig. 18(a)–(d) indicates that, without thermal stress, the HF is arrested at BPs and then diverted along it due to the relatively small vertical stress difference. When the temperature increases to 100 °C, the interaction mode does not change. However, at 200 °C and 300 °C, the interaction changes such that the HF activate the BPs and then cross them. Fig. 20 presents the temporal evolution of HF parameters. Changes in fracture height over time clearly illustrate two outcomes: arrest and crossing, and the variations in fracture length and width exhibit trends consistent with the previous results: higher temperature shortens the fracture while widening it.

Fig. 21 indicates the BP characteristics at the ($\sigma_v - \sigma_h$) of 2 MPa. At the same simulation time, a higher temperature results in a smaller activated area, while the opening width increases with temperature. Since BPs are activated, the pressure curves exhibit a plateau in the middle section. Increasing temperature leads to a reduction in plateau pressure, consistent with the previous findings. When the temperature exceeds 200 °C, after the BPs are crossed, both the opening range and the pressure influence range decrease slightly.

From the perspective of stress analysis, the transformation of the interaction mode can be explained as follows. Without thermal stress, a smaller vertical stress difference makes it easier for the fluid pressure to reach the threshold given by the sum of the normal stress and the tensile strength of the BP, leading to propagation along BPs. When the temperature rises to 100 °C, thermal stress is not strong enough to alter the interaction mode, but it reduces the normal stress acting on the BPs. Because heat exchange lags behind fracture propagation, the barrier to bedding-plane propagation remains largely unchanged as temperature rises. At the contact location between the HF and the BPs, thermal stress exerts a pronounced influence, causing a greater portion of the limited fluid energy to be consumed in enlarging the BP opening width rather than extending the fracture forward. As a result, the activated area of the BP is reduced relative to 20 °C, while the opening width is significantly larger. At 200 °C and 300 °C, the HF first propagates along the BPs during the initial intersection stage. As heat exchange progresses, thermal-stress effects at the contact point continue to intensify. Thermal stress not only reduces the normal stress acting on the BPs but also lowers the σ_h, thereby facilitating HF crossing of the BPs. Once the thermal stress effect enables the fluid pressure at the intersection to meet the conditions required for fracture crossing, the HF crosses the BPs, resulting in a scenario where it both activates and crosses them. After the BP is crossed, the activated area, the range of BP opening, and the pressure influence range change accordingly, corresponding to the variations observed in Fig. 21.

To more clearly illustrate the stress variations, the normal stress distributions above the BPs at 300 s under different temperatures were extracted along line L4, as well as the distributions of the σ_h above the bedding plane at 360 s and 780 s for the 300 °C case. As illustrated in Fig. 22(a), the normal stress distributions at different temperatures follow the same trend as in the 6 MPa case. As temperature rises, the normal stress on the BPs decreases, leading to an increase in opening width of BP and a reduction in fluid pressure. As the HF propagates along the BPs, heat exchange becomes increasingly sufficient and thermal-stress effect continue to intensify, as shown in Fig. 22(b). Consequently, the σ_h above the intersection between the HF and the BP continuously decreases, eventually allowing the HF to cross the BPs at the contact location.

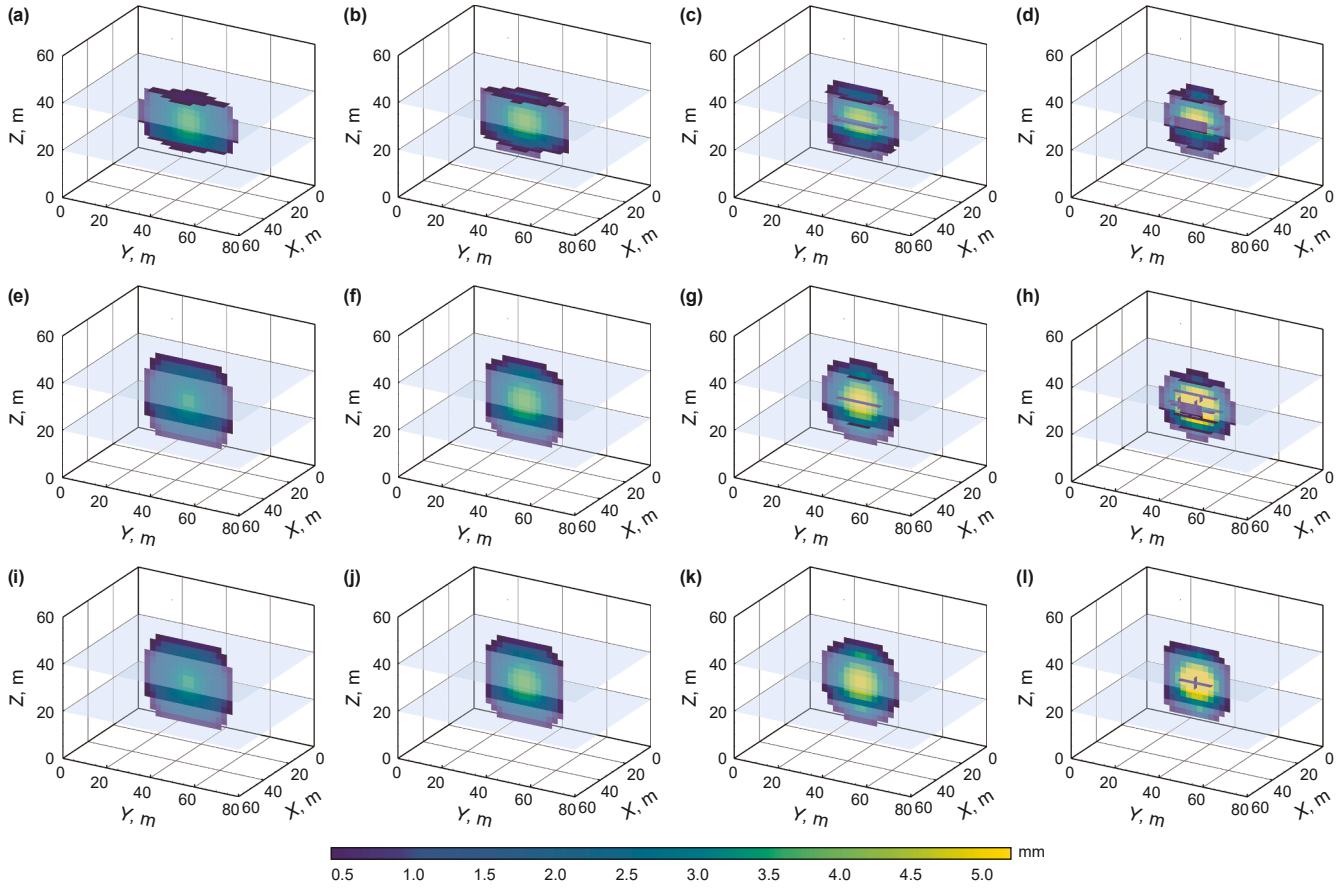


Fig. 18. Fracture width distributions for varying vertical stress differences and formation temperatures: (**a**) 2 MPa, 20 °C; (**b**) 2 MPa, 100 °C; (**c**) 2 MPa, 200 °C; (**d**) 2 MPa, 300 °C; (**e**) 6 MPa, 20 °C; (**f**) 6 MPa, 100 °C; (**g**) 6 MPa, 200 °C; (**h**) 6 MPa, 300 °C; (**i**) 12 MPa, 20 °C; (**j**) 12 MPa, 100 °C; (**k**) 12 MPa, 200 °C; (**l**) 12 MPa, 300 °C.

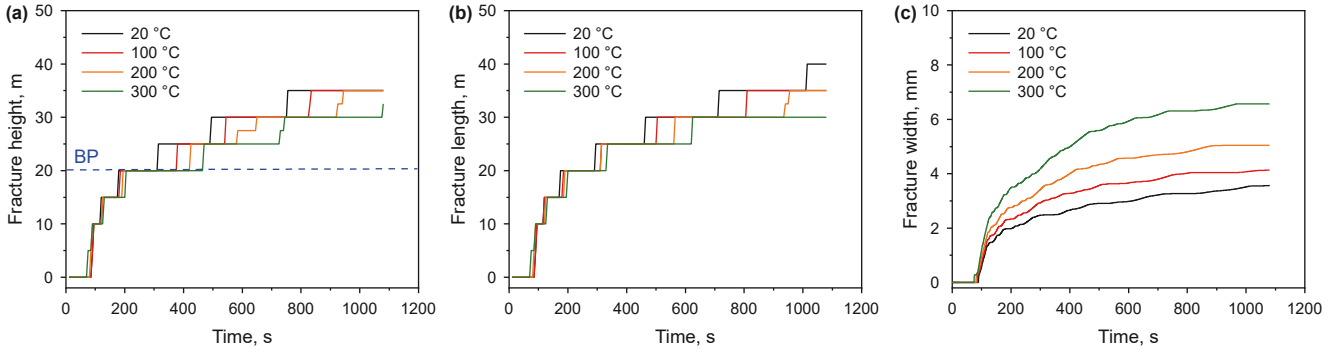


Fig. 19. The temporal evolution of HF parameters under 12 MPa and different temperatures: (**a**) HF height; (**b**) HF length; (**c**) injection point width.

From the research in this chapter, it can be known that in reservoirs with high temperature and α_T, the high thermal stress generated can promote the HFs that originally cross directly through the BPs to activate some of the BPs, and the HFs that originally expand along the BPs can cross the BPs, playing a significant positive role in the vertical extension of fractures and the formation of complex fracture networks. However, a high vertical stress difference will weaken the promoting effect of thermal stress on the activation of BPs.

5.3. The combined effect of the cohesion of BP and thermal stress

The cohesion and friction coefficient of the BP jointly determine its shear strength, which is a key factor controlling interaction behavior. In this section, based on simulation results under different BP cohesion (0, 2.5, and 5 MPa) and temperatures (20, 100, 200, and 300 °C), the combined effects of thermal stress and BP cohesion on the fracture height growth mechanisms and hydraulic fracture-bedding plane interaction behaviors are analyzed.

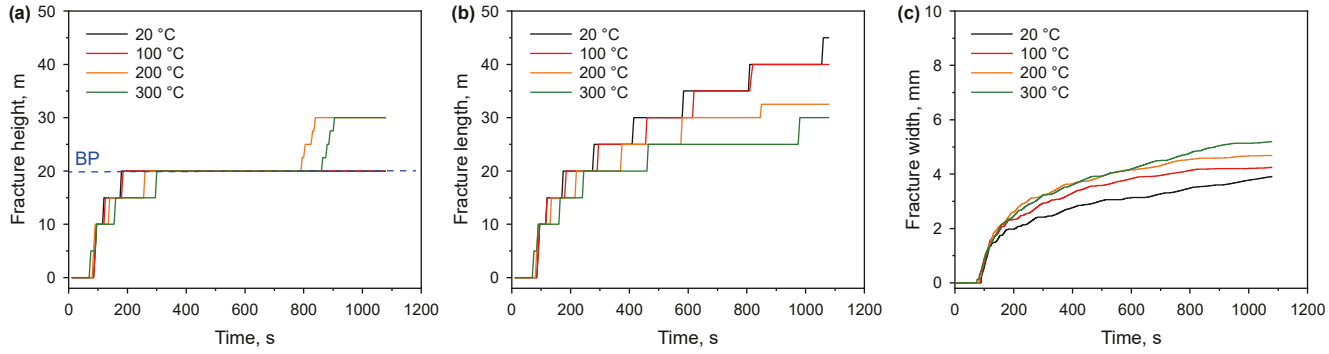


Fig. 20. The temporal evolution of HF parameters under 2 MPa and different temperatures: (**a**) HF height; (**b**) HF length; (**c**) injection point width.

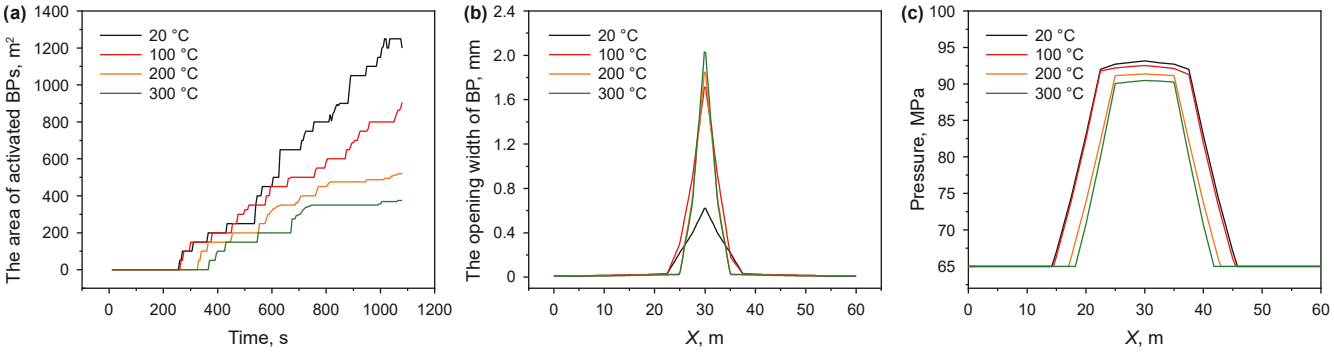


Fig. 21. The BP characteristics under different temperatures with 2 MPa: (**a**) activated area; (**b**) bedding plane opening width along line L3; (**c**) fluid pressure along line L3.

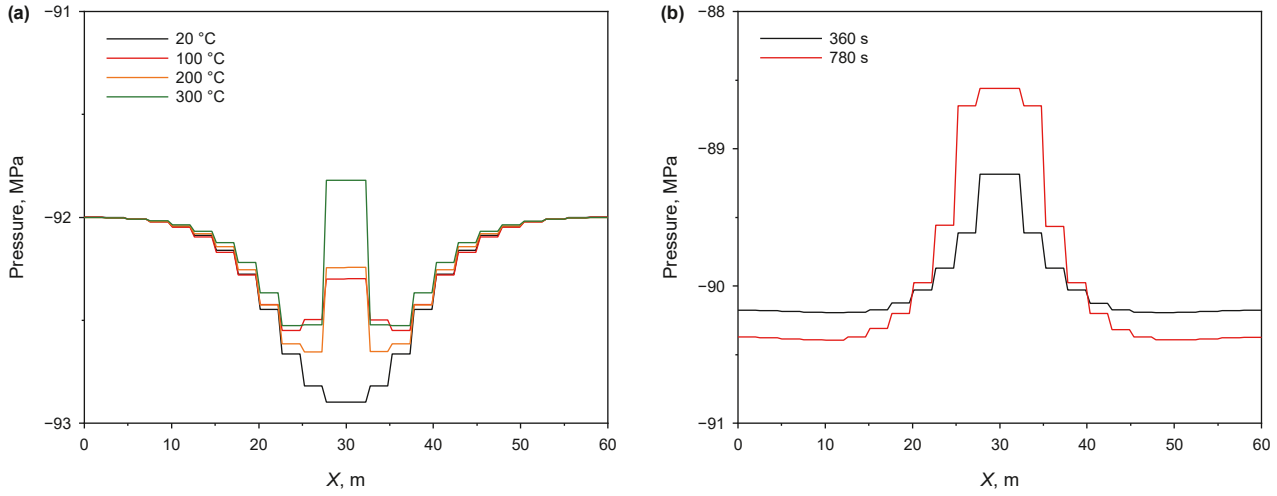


Fig. 22. (**a**) Normal stress distribution along line L4 at 300 s under different temperatures for the 2 MPa case; (**b**) minimum horizontal principal stress distribution along line L4 at 360 s and 780 s for the 300 °C case.

The remaining parameters are unaltered from Table 3. Fig. 23 compares fracture morphologies under different BP cohesions and formation temperatures.

The results for a BP cohesion of 2.5 MPa have been analyzed in the previous section. When the cohesion is 0 MPa, low interfacial shear strength makes it harder for the HF to cross BPs. As shown in Fig. 23(a)–(d), without considering thermal stress, the HF is arrested by the BPs. This is because high vertical stress inhibits BP opening, whereas low cohesion promotes shear failure along it. Therefore, once the fracture tip reaches the BP, preferential interfacial slip dissipates energy at the tip, ultimately arresting a fracture that could otherwise cross it. When the temperature increases to 100 °C, the HF crosses the BPs. This is because the presence of thermal stress reduces the σ_h above the BPs, making it easier for the HF to cross the BPs. Thus, although part of the energy is dissipated, HF eventually crosses the BPs. As temperature rises further, the BPs are progressively activated, with secondary fractures emerging. Fig. 24 presents the temporal evolution of HF parameters. Fig. 24(a) shows that, except at 20 °C, HF cross the BPs in all cases. Fracture height and length decrease as temperature

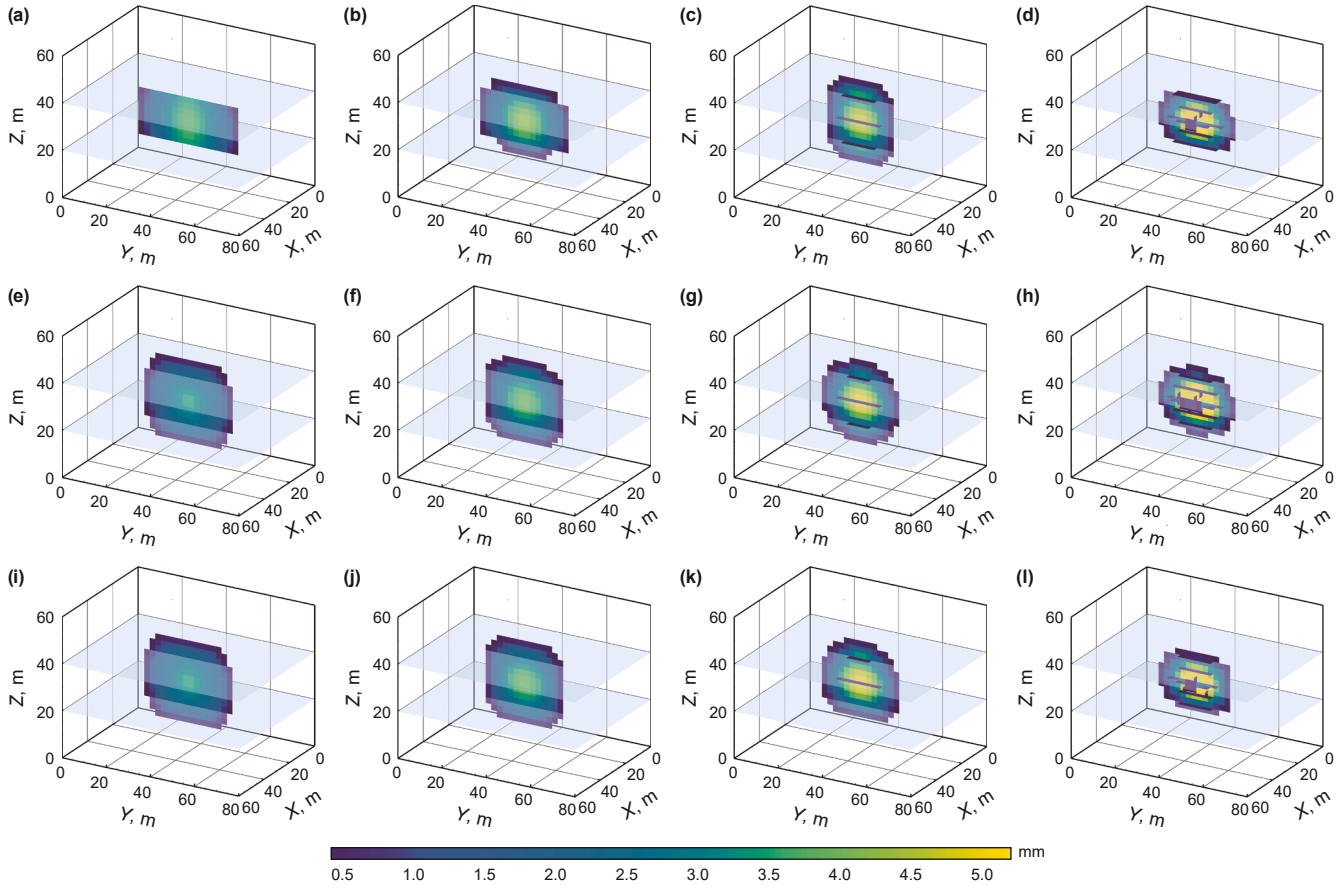


Fig. 23. Fracture width distributions under different BP's cohesion and temperatures: (**a**) 0 MPa, 20 °C; (**b**) 0 MPa, 100 °C; (**c**) 0 MPa, 200 °C; (**d**) 0 MPa, 300 °C; (**e**) 2.5 MPa, 20 °C; (**f**) 2.5 MPa, 100 °C; (**g**) 2.5 MPa, 200 °C; (**h**) 2.5 MPa, 300 °C; (**i**) 5 MPa, 20 °C; (**j**) 5 MPa, 100 °C; (**k**) 5 MPa, 200 °C; (**l**) 5 MPa, 300 °C.

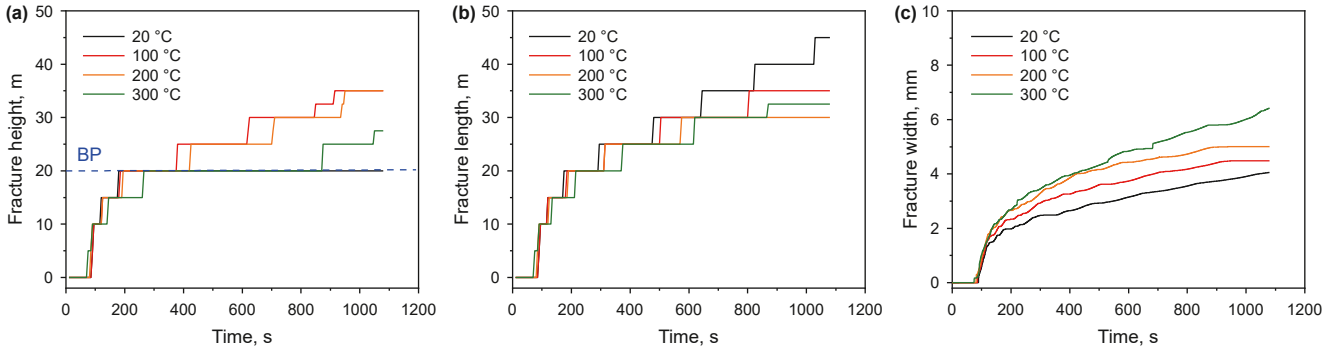


Fig. 24. The temporal evolution of HF parameters under cohesion 0 MPa and different temperatures: (**a**) HF height; (**b**) HF length; (**c**) injection point width.

rises, whereas fracture width increases markedly. When the cohesion increases to 5 MPa, the BPs are more likely to be crossed. The variation of the interaction mode with temperature exhibits a similar trend to that observed at a cohesion of 2.5 MPa. Therefore, the temporal evolution of fracture parameters is not discussed in detail here. However, the BP characteristics show certain differences, which will be compared with the cases of 0 MPa and 2.5 MPa in what follows.

The BP characteristics for a cohesion of 0 MPa are shown in Fig. 25. At 20 °C, the HF is arrested and BPs remain unopened, with most of the energy consumed by shear slip along the interface. As a result, the influence range of fluid pressure is relatively large. After the HF crosses the BPs, the overall trend becomes similar to that observed for cases without cohesion reduction: with increasing temperature, the BPs gradually open, the activated area expands, the opening width and range increase, and the fluid pressure on the BPs decreases slightly.

Fig. 26 shows the BP characteristics at 300 °C under different cohesion. As the cohesion decreases, shear deformation along the bedding interface occurs more easily, allowing the fluid energy to be more readily dissipated along the interface. This facilitates the opening width of the BP, thereby increasing both the activated area

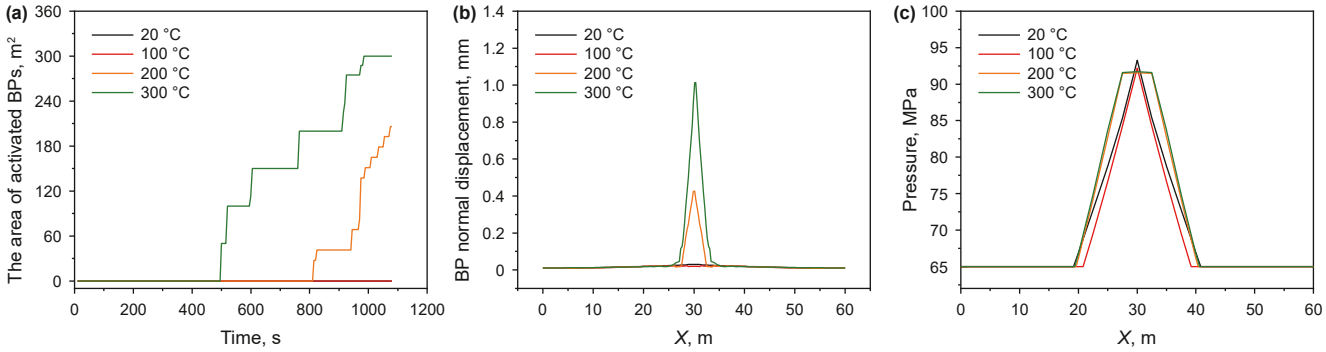


Fig. 25. The BP characteristics under different temperatures with cohesion 0 MPa: (**a**) activated area; (**b**) bedding plane opening width along line L3; (**c**) fluid pressure along line L3.

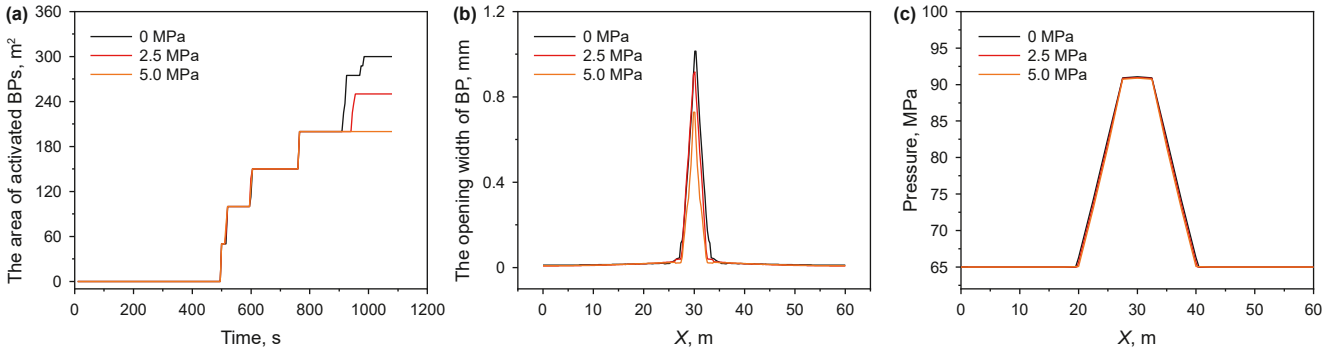


Fig. 26. The BP characteristics at 300 °C under different cohesion: (**a**) activated area; (**b**) bedding plane opening width along line L3; (**c**) fluid pressure along line L3.

and the opening width. As shown in Fig. 23, when the cohesion increases from 0 to 5 MPa, the activated area decreases from 300 m^2 to 200 m^2, the maximum opening decreases from 1.01 mm to 0.73 mm, the opening range decreases from 5.27 m to 3.78 m, and the pressure influence range contracts from 21.2 m to 20 m, all showing a consistent decreasing trend.

6. Discussion

For deep shale reservoirs, the vertical stress difference is generally high. It is commonly considered that HFs tend to propagate across BPs under such conditions, resulting in relatively simple fracture geometries and making it difficult to form complex fracture networks. The results of this study demonstrate that thermal stress can play a key regulatory role in fracture propagation, and temperature effects should not be neglected in deep, high-temperature reservoirs. Under the influence of thermal stress, HF may activate BPs, thereby altering the conventional crossing-dominated propagation mode, and improving reservoir stimulation efficiency. Therefore, in practical hydraulic fracturing design, reservoirs with relatively lower vertical stress difference and certain temperature conditions may be preferentially considered to achieve more favorable fracture propagation behavior.

It should be noted that the interaction behavior between hydraulic fractures and bedding planes is governed by multiple factors. The present study focuses on the underlying mechanisms, and the parameter combinations and ranges corresponding to bedding plane activation under different geological conditions still need to be further clarified through more systematic parametric analyses. This will enable the development of engineering-oriented criteria or design charts, which is an important extension of this work and will be addressed in future studies.

In actual reservoirs, geological conditions are more complex. Vertically, multiple BPs may exist, often accompanied by interlayers or reservoirs with varying physical properties; along the fracture propagation direction, NFs with different orientations and scales may also be present. All these factors can influence fracture propagation behavior. The model established in this study is primarily intended for mechanism analysis of fracture propagation. To highlight the effects of key factors, a relatively simplified fracture–bedding model is adopted. This simplification facilitates the isolation of controlling factors and systematic analysis; however, it differs from actual reservoir conditions. Direct application of such a simplified model to field-scale fracture prediction may introduce errors. Nevertheless, the proposed model has good extensibility. On this basis, multiple bedding layers, complex natural fractures, and heterogeneous formation conditions can be further incorporated to construct a numerical model that is closer to actual geological conditions, thereby enabling prediction of fracture propagation behavior in actual reservoirs and providing support for fracture height control and hydraulic fracturing design.

Previous studies have shown that differences in reservoir properties between layers above and below the BP (such as elastic modulus and in-situ stress) can also significantly affect the interaction between HFs and BPs; however, this factor is not considered in the present manuscript. Therefore, future work will further investigate the interaction mechanisms between HFs and BPs under the combined effects of thermal stress and interlayer property contrasts. In addition, with increasing reservoir depth, both temperature and pressure rise, and the rock may exhibit elastoplastic behavior. The present model is based on linear elasticity and does not account for the influence of elastoplastic

deformation on fracture propagation. Therefore, developing a thermo-hydro-mechanical fracture propagation model that incorporates elastoplastic behavior will be a focus of our future work.

7. Conclusions

Based on the established three-dimensional thermo-hydro-mechanical coupled hydraulic fracturing model (CDEM-THM), this study investigates the fracture height growth mechanisms and hydraulic fracture-bedding plane interaction behaviors under the combined effects of thermal stress (reservoir temperature and thermal expansion coefficient), vertical stress difference, and bedding plane cohesion. The following conclusions can be drawn:

(1) The thermal stress induced by injecting low-temperature fluid into a high-temperature reservoir significantly alters the original in-situ stress field, serving as a key factor controlling the fracture height growth and hydraulic fracture-bedding plane interaction behaviors.
(2) Thermal stress acts in the form of tensile stress, reduces the three in-situ principal stresses, and lowers the fracturing pressure. As reservoir temperature and thermal expansion coefficient increase, the thermal stress intensifies, resulting in a significant enlargement of fracture width, reductions in fracture height and length, and the formation of secondary fractures on both sides of the main fracture, leading to a more complex fracture geometry.
(3) Thermal stress reduces the normal stress above bedding planes, thereby lowering the difficulty of bedding-plane activation. As temperature increases, the hydraulic fracture-bedding plane interaction behavior shifts from pure crossing to crossing with partial activation, accompanied by enlarged activated areas and greater opening widths, which is conducive to the formation of a complex fracture network. However, with increasing vertical stress difference, bedding planes become difficult to activate even at high temperatures, as a large stress difference weakens the promoting effect of thermal stress on bedding activation.
(4) When the vertical stress difference is small, the promoting effect of thermal stress on the fracture's ability to cross bedding planes becomes more pronounced. With increasing temperature, the minimum horizontal principal stress above the hydraulic fracture-bedding plane intersection continues to decrease, and the interaction mode gradually changes from propagation along the bedding plane to activation and crossing of the bedding plane, which plays a positive role in the vertical extension of hydraulic fractures.
(5) When the bedding plane cohesion is low, the interface is prone to shear slip, and the hydraulic fracture is arrested at the bedding plane under non-thermal conditions. With increasing temperature, thermal stress enables the fracture to cross and partially activate the bedding plane. As cohesion increases, interface strength and confinement are enhanced, thereby weakening the promoting effect of thermal stress on bedding activation, leading to reductions in both activated area and opening width.

CRediT authorship contribution statement

Hai-Yang Wang: Writing – review & editing, Writing – original draft, Validation, Data curation, Conceptualization. **Ming Chen:** Writing – original draft, Project administration, Methodology, Conceptualization. **Tian-Kui Guo:** Software, Investigation, Funding acquisition. **Yi Zhang:** Supervision, Resources, Conceptualization. **Ji-Wei Wang:** Methodology, Formal analysis. **Xin-Min Ge:** Project administration, Formal analysis. **Bo Chen:** Project administration, Methodology. **Feng-Shou Zhang:** Methodology.

Conflict of interest

The authors declare that they have no known competing financial interests or personal relationships that could have appeared to influence the work reported in this paper.

Acknowledgment

The authors would like to acknowledge the financial support of the National Natural Science Foundation of China (Grand No. 52288101) and the Fundamental Research Funds for the Central Universities (23CX06006A).

References

Barends, F.B., 2010. Complete solution for transient heat transport in porous media, following Lauwerier's concept. In: SPE Annual Technical Conference and Exhibition 2010, SPE-134670-MS. https://doi.org/10.2118/134670-MS.
Cong, Z.-Y., Li, Y.-W., Tang, J.-Z., et al., 2022. Numerical simulation of hydraulic fracture height layer-through propagation based on three-dimensional lattice method. Eng. Fract. Mech. 264, 108331. https://doi.org/10.1016/j.engfracmech.2022.108331.
Dontsov, E.V., 2016. An approximate solution for a penny-shaped hydraulic fracture that accounts for fracture toughness, fluid viscosity and leak-off. R. Soc. Open Sci. 3 (12), 160737. https://doi.org/10.1098/rsos.160737.
Feng, C., Li, S.-H., Zheng, B.-X., et al., 2019. Numerical simulation on complete process of three-dimensional bench blasting in an open-pit mine based on CDEM. Explos. Shock Waves 39 (2), 110–120. https://doi.org/10.11883/bzycj-2017-0393 (in Chinese).
Gao, Q., Ahmad, Ghassemi, 2020. Height growth in layered unconventional reservoirs: The impact of formation moduli, interfaces, and in-situ stress. SPE Prod. Oper. 35 (4), 756–774. https://doi.org/10.15530/urtec-2019-6.
Gu, H., Weng, X., Lund, J., et al., 2012. Hydraulic fracture crossing natural fracture at nonorthogonal angles: A criterion and its validation. SPE Prod. Oper. 27 (01), 20–26. https://doi.org/10.2118/139984-PA.
Guo, T.-K., Wang, H.-Y., Chen, M., et al., 2025. Numerical simulation of fracture propagation in deflagration-hydraulic composite fracturing of unconventional reservoirs. Petrol. Explor. Dev. 52 (4), 1017–1028. https://doi.org/10.1016/S1876-3804(25)60619-7.
Jiao, K.-T., Han, D.-X., Li, J.-F., et al., 2021. A novel LBM-DEM based pore-scale thermal-hydro-mechanical model for the fracture propagation process. Comput. Geotech. 139, 104418. https://doi.org/10.1016/j.compgeo.2021.104418.
Ju, Y., Liu, P., Chen, J.-L., et al., 2016. CDEM-based analysis of the 3D initiation and propagation of hydrofracturing cracks in heterogeneous glutenites. J. Nat. Gas Sci. Eng. 36, 614–623. https://doi.org/10.1016/j.jngse.2016.09.011.
Lauwerier, H.A., 1955. The transport of heat in an oil layer caused by the injection of hot fluid. Appl. Sci. Res. Section A 5, 145–150.
Lei, Q., Weng, D.-W., Xiong, S.-C., et al., 2021. Progress and development directions of shale oil reservoir stimulation technology of China National Petroleum Corporation. Petrol. Explor. Dev. 48 (5), 1198–1207. https://doi.org/10.1016/S1876-3804(21)60102-7.
Li, S.-B., Zhang, D.-X., 2023. Three-dimensional thermoporoelastic modeling of hydrofracturing and fluid circulation in hot dry rock. J. Geophys. Res. Solid Earth 128 (2), e2022JB025673. https://doi.org/10.1029/2022JB025673.
Li, X.-W., Hu, Y.-Q., Wang, Q., et al., 2025. Propagation law of fractures in deep shale gas reservoirs considering the influence of interlayers and interfaces. Phys. Fluids 37 (5). https://doi.org/10.1063/5.0272600.
Lin, R., Peng, S.-R., Zhao, J.-Z., et al., 2024. Multiple hydraulic fracture propagation simulation in deep shale gas reservoir considering thermal effects. Eng. Fract. Mech. 303, 110147. https://doi.org/10.1016/j.engfracmech.2024.110147.
Luo, Z.-F., Cheng, L., Zhao, L.-J., et al., 2022. Numerical simulation and analysis of thermo-hydro-mechanical behaviors of hydraulic fracturing in naturally fractured formation using a THM-XFEM coupling model. J. Nat. Gas Sci. Eng. 103, 104657. https://doi.org/10.1016/j.jngse.2022.104657.
Martyushev, D.A., Yang, Y.-F., Kazemzadeh, Y., et al., 2024. Understanding the mechanism of hydraulic fracturing in naturally fractured carbonate reservoirs: Microseismic monitoring and well testing. Arabian J. Sci. Eng. 49 (6), 8573–8586. https://doi.org/10.1007/s13369-023-08513-1.
Nie, H.-K., Jin, Z.-J., Li, P., et al., 2023. Deep shale gas in the Ordovician-Silurian Wufeng–Longmaxi formations of the Sichuan Basin, SW China: Insights from reservoir characteristics, preservation conditions and development strategies. J. Asian Earth Sci. 244, 105521. https://doi.org/10.1016/j.jseaes.2022.105521.

Qu, H., Li, Z.-L., Li, C.-Y., et al., 2023. Experimental study of fracture initiation and morphology in low-brittle shales with bedding planes subjected to LN fracturing. Rock Mech. Rock Eng. 56, 6299–6319. https://doi.org/10.1007/s00603-023-03407-y.

Qu, H., Tang, S.-M., Liu, Y., et al., 2022. Characteristics of complex fractures by liquid nitrogen fracturing in brittle shales. Rock Mech. Rock Eng. 55, 1807–1822. https://doi.org/10.1007/s00603-021-02767-7.

Ren, Q.-S., Zhao, Y.-X., Zhu, X.-G., et al., 2022. CDEM-based simulation of the 3D propagation of hydraulic fractures in heterogeneous coalbed methane reservoirs. Comput. Geotech. 152, 104992. https://doi.org/10.1016/j.compgeo.2022.104992.

Savitski, A.A., Detournay, E., 2002. Propagation of a penny-shaped fluid-driven fracture in an impermeable rock: Asymptotic solutions. Int. J. Solid Struct. 39 (26), 6311–6337. https://doi.org/10.1016/S0020-7683(02)00492-4.

Taleghani, A.D., Gonzalez, M., Shojaei, A., 2016. Overview of numerical models for interactions between hydraulic fractures and natural fractures: Challenges and limitations. Comput. Geotech. 71, 361–368. https://doi.org/10.1016/j.compgeo.2015.09.009.

Wang, D.-B., Zhou, F.-J., Li, Y.-P., et al., 2022a. Numerical simulation of fracture propagation in Russia carbonate reservoirs during refracturing. Pet. Sci. 19 (6), 2781–2795. https://doi.org/10.1016/j.petsci.2022.05.013.

Wang, J.-W., Qu, Z.-Q., Guo, T.-K., et al., 2022b. Numerical simulation of hydraulic fracturing damage evolution in geothermal reservoirs with natural fractures based on THMD coupling model. In: 56th U.S. Rock Mechanics/Geomechanics Symposium, ARMA-2022-0951. https://doi.org/10.56952/ARMA-2022-0951.

Wang, J.-W., Guo, T.-K., Chen, M., et al., 2024. Numerical simulation of fracture propagation morphology in hydraulic fracturing development of geothermal reservoirs based on the CDEM-THM3D. Comput. Geotech. 172, 106444. https://doi.org/10.1016/j.compgeo.2024.106444.

Xie, Z.-X., Huang, Z.-W., Sun, Z.-W., et al., 2025. The interaction behaviors between the hydraulic fracture and natural fracture in hot dry rock. Geoenergy Sci. Eng. 247, 213731. https://doi.org/10.1016/j.geoen.2025.213731.

Zeng, Q.-D., Yao, J., Shao, J.-F., 2020. An extended finite element solution for hydraulic fracturing with thermo-hydro-elastic–plastic coupling. Comput. Methods Appl. Mech. Eng. 364, 112967. https://doi.org/10.1016/j.cma.2020.112967.

Zhang, B., Guo, T.-K., Chen, M., et al., 2025. Research on hydraulic fracture propagation and interwell interference mechanisms during multi-well pad fracturing in shale reservoirs. Eng. Geol. 346, 107905. https://doi.org/10.1016/j.enggeo.2025.107905.

Zhang, B., Guo, T.-K., Qu, Z.-Q., et al., 2023. Numerical simulation of fracture propagation and production performance in a fractured geothermal reservoir using a 2D FEM-Based THMD coupling model. Energy 273, 127175. https://doi.org/10.1016/j.energy.2023.127175.

Zhang, Y.-H., Guo, T.-K., Chen, M., et al., 2024. Numerical simulation study of fracture height growth considering the influence of bedding planes. Comput. Geotech. 168, 106144. https://doi.org/10.1016/j.compgeo.2024.106144.

Zhang, Q., Zhang, X.-P., Sun, W., 2021. A review of laboratory studies and theoretical analysis for the interaction mode between induced hydraulic fractures and pre-existing fractures. J. Nat. Gas Sci. Eng. 86, 103719. https://doi.org/10.1016/j.jngse.2020.103719.

Zhao, J.-Z., Ren, L., Lin, C., et al., 2025. A review of deep and ultra-deep shale gas fracturing in China: Status and directions. Renew. Sustain. Energy Rev. 209, 115111. https://doi.org/10.1016/j.rser.2024.115111.

Zhou, T., Wang, H.-B., Li, F.-X., et al., 2020. Numerical simulation of hydraulic fracture propagation in laminated shale reservoirs. Petrol. Explor. Dev. 47 (5), 1117–1130. https://doi.org/10.1016/S1876-3804(20)60122-7.

Zhu, X.-G., Feng, C., Cheng, P.-D., et al., 2021. A novel three-dimensional hydraulic fracturing model based on continuum–discontinuum element method. Comput. Methods Appl. Mech. Eng. 383, 113887. https://doi.org/10.1016/j.cma.2021.113887.

Zou, C.-N., Zhao, Q., Cong, L.-Z., et al., 2021. Development progress, potential and prospect of shale gas in China. Nat. Gas. Ind. 41, 1–14. https://doi.org/10.3787/j.issn.1000-0976.2021.01.001 (in Chinese).

Zou, Y.-S., Ma, X.-F., Zou, T., et al., 2017. Hydraulic fracture growth in a layered formation based on fracturing experiments and discrete element modeling. Rock Mech. Rock Eng. 50, 2381–2395. https://doi.org/10.1007/s00603-017-1241-z.